Loss of the *N*-acetylgalactosamine side chain of the GPI-anchor impairs bone formation and brain functions and accelerates the prion disease pathology

Tetsuya Hirata[1], Atsushi Kobayashi[2], Tamio Furuse[3], Ikuko Yamada[3], Masaru Tamura[3], Hiroyuki Tomita[4], Yuko Tokoro[1], Akinori Ninomiya[5], Yoshitaka Fujihara[6], Masahito Ikawa[6], Yusuke Maeda[7,8], Yoshiko Murakami[7,8], Yasuhiko Kizuka[1,*], and Taroh Kinoshita[7,8,*]

From the [1]Institute for Glyco-core Research (iGCORE), Gifu University, Gifu, Japan; [2]Laboratory of Comparative Pathology, Faculty of Veterinary Medicine, Hokkaido University, Sapporo, Hokkaido, Japan; [3]Technology and Development Team for Mouse Phenotype Analysis, RIKEN BioResource Research Center, Tsukuba, Ibaraki, Japan; [4]Department of Tumor Pathology, Graduate School of Medicine, Gifu University, Gifu, Japan; [5]Core Instrumentation Facility, [6]Department of Experimental Genome Research, [7]Yabumoto Department of Intractable Disease Research, Research Institute for Microbial Diseases, and [8]WPI Immunology Frontier Research Center, Osaka University, Suita, Osaka, Japan

Edited by Gerald Hart

Glycosylphosphatidylinositol (GPI) is a posttranslational glycolipid modification of proteins that anchors proteins in lipid rafts on the cell surface. Although some GPI-anchored proteins (GPI-APs), including the prion protein PrP^C, have a glycan side chain composed of *N*-acetylgalactosamine (Gal-NAc)–galactose–sialic acid on the core structure of GPI glycolipid, *in vivo* functions of this GPI-GalNAc side chain are largely unresolved. Here, we investigated the physiological and pathological roles of the GPI-GalNAc side chain *in vivo* by knocking out its initiation enzyme, PGAP4, in mice. We show that *Pgap4* mRNA is highly expressed in the brain, particularly in neurons, and mass spectrometry analysis confirmed the loss of the GalNAc side chain in PrP^C GPI in PGAP4-KO mouse brains. Furthermore, PGAP4-KO mice exhibited various phenotypes, including an elevated blood alkaline phosphatase level, impaired bone formation, decreased locomotor activity, and impaired memory, despite normal expression levels and lipid raft association of various GPI-APs. Thus, we conclude that the GPI-GalNAc side chain is required for *in vivo* functions of GPI-APs in mammals, especially in bone and the brain. Moreover, PGAP4-KO mice were more vulnerable to prion diseases and died earlier after intracerebral inoculation of the pathogenic prion strains than wildtype mice, highlighting the protective roles of the GalNAc side chain against prion diseases.

Addition of glycosylphosphatidylinositol (GPI) to proteins is a posttranslational modification of proteins widely conserved among eukaryotes (1, 2). Approximately 150 types of mammalian proteins, including Thy1, 120-kDa neural cell adhesion molecule (NCAM120), alkaline phosphatases (ALPs), and prion protein (PrP^C), are modified by GPI and expressed in lipid rafts (usually defined as a detergent-resistant membrane [DRM]) on the cell surface through GPI (3). These GPI-anchored proteins (GPI-APs) fulfill significant roles in early development, synaptic formation, and immunological regulation. Mammalian GPI is composed of a common core structure, EtNP-6Manα1–2Manα1–6(EtNP)Man-α1–4GlcNα1–6*myo*inositol-phospholipid (where EtNP, Man, and GlcN are ethanolamine phosphate, mannose, and glucosamine, respectively, Fig. 1A) (1, 2). The mammalian GPI core structure can be further modified with various side chains. One modification is the linking of the fourth Man to the third Man *via* an α1,2 linkage (4), whereas the other is the attachment of the GalNAc side chain, which is composed of at most three sugar residues, to the first Man residue. The structure of the GalNAc side chain is Neu5-Acα2–3Galβ1–3GalNAcβ1–4(Man) (where Neu5Ac, Gal, and GalNAc are *N*-acetylneuraminic acid, galactose, and *N*-acetylgalactosamine, respectively, Fig. 1A) (5–7). These side chains provide structural diversity to GPI-glycans.

The biosynthesis of GPI starts in the endoplasmic reticulum (ER). Sugars and EtNP moieties are sequentially added to a phosphatidylinositol by step-wise reactions, and complete GPI precursors are generated, followed by *en bloc* transfer of the GPI moiety to proteins by GPI transamidase, generating nascent GPI-APs (1, 2). GPI-glycan and -lipid structures of nascent GPI-APs are then remodeled in the ER and Golgi to complete GPI maturation (1, 2). Although the biosynthetic pathway of the core GPI is well characterized, biosynthesis of the GPI-GalNAc side chain has not been studied for over 30 years since the complete chemical structure of mammalian GPI, including GalNAc addition, was reported in 1988 (5). We recently identified post-GPI attachment to proteins factor 4 (PGAP4, also known as TMEM246), a GPI-specific GalNAc transferase that catalyzes the first reaction for generating the GalNAc side chain (Fig. 1A) (8). PGAP4 has weak homology to GnT-IVa, an *N*-acetylglucosaminyltransferase for *N*-glycan branching, and uniquely has three transmembrane domains (8). More recently, we identified B3GALT4 as the Gal

* For correspondence: Yasuhiko Kizuka, kizuka@gifu-u.ac.jp; Taroh Kinoshita, tkinoshi@biken.osaka-u.ac.jp.
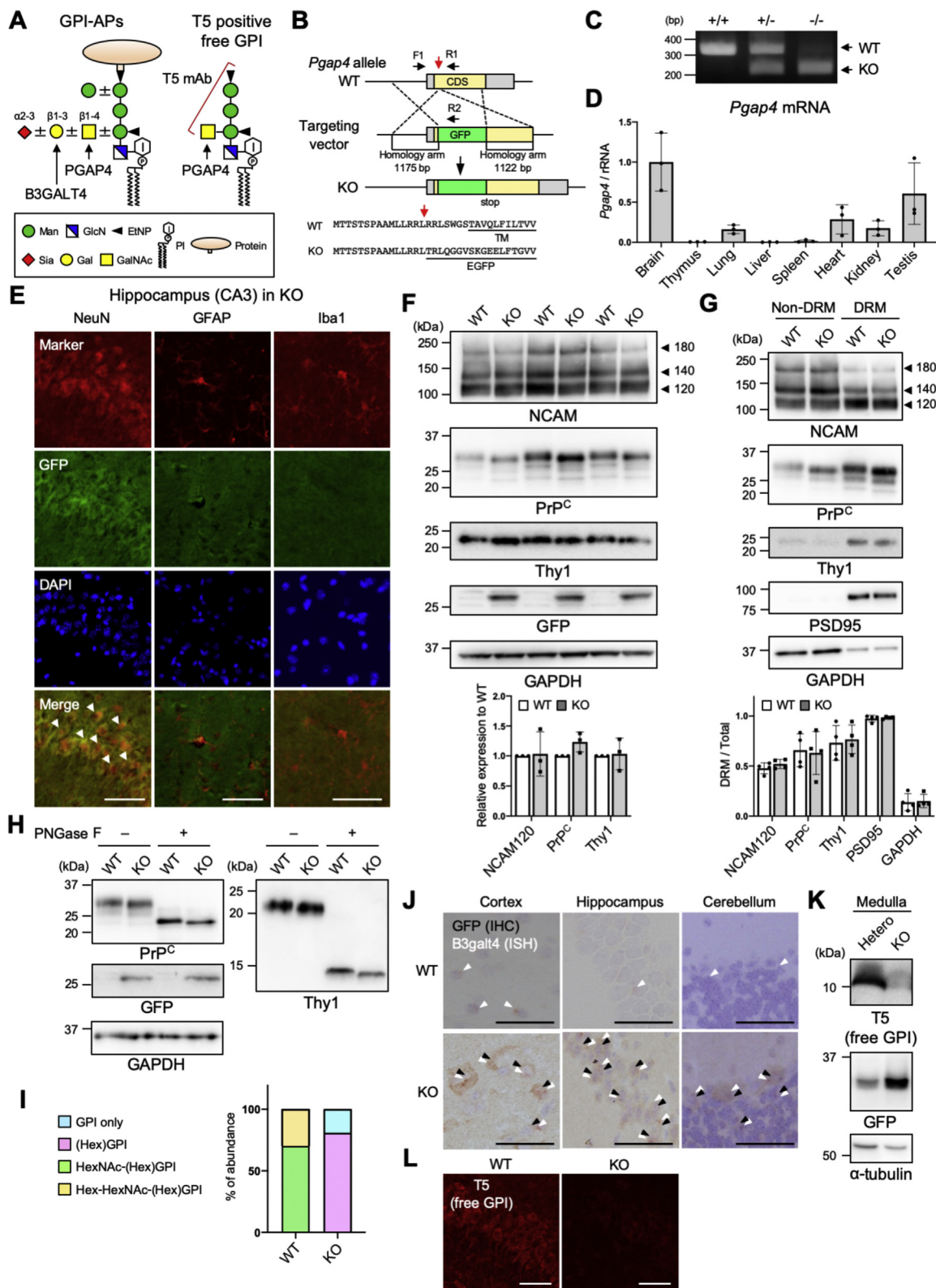
Figure 1. Loss of GPI GalNAc side chain in PGAP4-KO mice. *A*, schematics of GPI-APs and free GPI with GalNAc side chain are shown. T5 monoclonal antibody (mAb) detects free GPI modified with GalNAc. *B*, *top*, schematic of generation of PGAP4-KO mouse. *EGFP* sequence is inserted by homologous recombination into *Pgap4* allele, which is digested by CRISPR-Cas9 (*red arrow*) in ES cells. *Bottom*, amino acid sequence of WT and mutant PGAP4 are shown. A *red arrow* indicates the position of amino acid whose coding genome sequence was digested by CRISPR-Cas9. *C*, genotyping of PGAP4-KO mice. The DNA fragments in *Pgap4* allele were amplified with primers indicated in *B* (F1, R1, and R2); F1 and R1 for WT, F1 and R2 for KO. *D*, mRNA of *Pgap4* was measured in eight tissues (brain, thymus, lung, liver, spleen, heart, kidney, and testis) in WT mice (*n* = 3). The expression levels of *Pgap4* mRNA were normalized by those of rRNA. *E*, immunofluorescence images of mouse hippocampus (CA3) with anti-GFP (PGAP4 expressing cells) and anti-NeuN (neurons), anti-GFAP (astrocytes), or anti-Iba1 (microglia), respectively. These are magnified images of Fig. S1*B*. *White arrowhead* indicated the cells costained with GFP and neuronal markers. The scale bar represents 50 μm. *F*, whole-brain lysates from three WT and PGAP4-KO mice were blotted for NCAM, PrP^C, Thy1, GFP, and

transferase for the GPI side chain (Fig. 1A) (9). In contrast to PGAP4, B3GALT4 is involved in biosynthesis of not only GPI but also GM1, another type of glycolipid (10, 11). We also showed that sialic acid of the GPI side chain of human brain PrP^C is attached *via* an α2,3-linkage (7). These studies have largely elucidated the structure and the biosynthetic pathway of the GPI-GalNAc side chain.

Several lines of studies using knockout (KO) mice of GPI biosynthetic genes have revealed the physiological significance of the core structure of GPI and remodeling of GPI. Loss of GPI-APs or abnormal GPI structures cause severe phenotypes, including early embryonic lethality (12), facial dysmorphisms such as otocephaly (13–15) and cleft-lip palate (16), male infertility (13), abnormal immune responses (17), and neuronal dysfunctions (18, 19). In addition, recent genetic studies have reported patients with inherited GPI deficiency (IGD) who have genetic mutations in GPI biosynthetic genes, including GPI remodeling enzymes. The main symptoms of patients with IGD are intellectual disability, developmental delay, and epilepsy (20, 21). Other symptoms seen in patients with IGD are brain anomalies (such as delayed myelination, cerebral atrophy, and hypoplasia of the cerebellum), dysmorphic facial features, malformations, hyperphosphatasia, skeletal abnormalities (such as scoliosis, osteoporosis, and reduced mineralization), organ anomalies (such as cardiac, gastrointestinal, and muscular anomalies), and deafness (22–27). These lines of evidence clearly demonstrate that GPI is vitally important for development and various physiological functions, and not only loss of GPI-AP expression but also abnormal GPI structures cause severe disorders. These findings suggest that GPI side chains, including the GalNAc side chain, also play significant functional roles *in vivo*. However, the *in vivo* functions of the GPI-GalNAc side chain remain unknown.

Prion diseases, including Creutzfeldt–Jakob disease and Gerstmann–Sträussler–Scheinker (GSS) syndrome in humans and scrapie, bovine spongiform encephalopathy, and chronic wasting syndrome in animals, are lethal, transmissible, and progressive neurodegenerative disorders (28, 29). Prion diseases are caused by the accumulation of the disease type of prion protein (scrapie form of the prion protein, PrP^{Sc}), which is converted from normal prion protein (cellular prion protein, PrP^C) (28). Although the conversion mechanisms of PrP^C to PrP^{Sc} remain largely unknown, the structural features of PrP^C and PrP^{Sc} are well described with α-helix-rich and β-sheet-rich structures, respectively (28, 30). KO mice of the *Prnp* gene, encoding PrP^C, are resistant to the prion disease even after inoculation with PrP^{Sc} (31, 32), demonstrating that the presence of PrP^C is critical for the pathogenesis of prion diseases. Furthermore, knocking out *Prnp* in neurons after inoculation

of PrP^{Sc} strains prevents further conversion of PrP^C to PrP^{Sc} in neurons and rescues neurodegeneration caused by the PrP^{Sc} infection (33). Mice even showed persistent gliosis because of PrP^{Sc} accumulation in astrocytes and microglia (33). Therefore, preventing PrP^{Sc} formation in neurons represents a robust potential therapeutic approach against prion diseases for which no clinical treatment exists.

A recent study suggested that the pathology of prion diseases arises from two distinct mechanisms: the conversion of PrP^C to PrP^{Sc} and the neurotoxic signaling from PrP^{Sc} (34). Previous evidences have shown that the GPI of PrP^C is involved in the pathology of prion diseases through both mechanisms (35). For example, the lifespan of transgenic mice expressing GPI-anchorless PrP^C was greatly prolonged after inoculation with PrP^{Sc} and persistent accumulation of PrP^{Sc} (36–38), suggesting that neurotoxicity of PrP^{Sc} depends on membrane anchoring of PrP^{Sc} through GPI. Furthermore, an *in vitro* study using cultured neurons showed that PrP^C with desialylated GPI is resistant to conversion to PrP^{Sc} (39). The results from another study suggested that mice expressing PrP^C with less sialylated GPI have a prolonged incubation period after challenging with PrP^{Sc} because of the reduction in PrP^{Sc} accumulation and intracellular signaling (40). These studies suggest that the GPI-anchor affects the conversion process of PrP^C to PrP^{Sc}. The recent identification of the biosynthetic enzymes for the GalNAc side chain enables us to investigate whether the GPI-GalNAc side chain is involved in the pathology of prion diseases *in vivo*.

In this study, we aimed to understand *in vivo* functions of the GPI-GalNAc side chain in normal and disease states. For this purpose, we generated PGAP4-KO (*Pgap4$^{-/-}$*) mice and performed biochemical and behavioral tests. In addition, we intracerebrally inoculated PrP^{Sc} in PGAP4-KO mice and measured their lifespan. We reveal that PGAP4-KO mice exhibit various phenotypes and progress of the pathology of prion disease. Thus, our study uncovers the physiological and pathological significance of the GPI-GalNAc side chain.

Results

Generation of PGAP4-KO mice

PGAP4-KO mice were generated to elucidate the physiological and pathological roles of the GPI-GalNAc side chain. We designed the KO construct by in-frame insertion of the *EGFP* sequence into the *Pgap4* allele to disrupt PGAP4 expression and to express EGFP under the *Pgap4* promoter to detect endogenously PGAP4-expressing cells and tissues (Fig. 1B). The *Pgap4* allele was digested with the CRISPR-Cas9 system (41, 42) in ES cells cotransfected with a targeting vector

---

GAPDH. The graph showed the relative band intensities of GPI-APs in PGAP4-KO mice to WT mice normalized by GAPDH ($n = 3$). Statistics was calculated by Welch's *t* test. *G*, Triton X-100-soluble (non-DRM) and insoluble (DRM) fractions were blotted for NCAM, PrP^C, Thy1, PSD95, and GAPDH. The graph showed the ratio of DRM-associated proteins ($n = 4$). Statistics was calculated by unpaired Student's *t* test. *H*, brain lysates from WT and PGAP4-KO mice were treated with or without PNGase F and blotted for PrP^C, Thy1, GFP, and GAPDH. *I*, LC-electrospray ionization-MS of PrP^C purified from WT and PGAP4-KO mouse brains. Percentage of detected GPI species are shown in the graph. *J*, the brain sections were double stained with anti-GFP and *in situ* hybridization probe for *B3galt4* mRNA. *Black* and *white arrowheads* indicate the signals of GFP and *B3galt4* mRNA, respectively. The scale bar represents 50 μm. *K*, lysates of medulla oblongata from PGAP4-hetero and PGAP4-KO mice were blotted for free GPI with GalNAc (detected by anti-T5), GFP, and α-tubulin. *L*, immunofluorescence images of mouse hippocampus (CA3) with anti-T5. The scale bar represents 50 μm.

SASBMB

J. Biol. Chem. (2022) 298(3) 101720 **3**

with the *EGFP* sequence and homology arms of the *Pgap4* sequence (Fig. 1*B*). ES cells with the *EGFP* sequence correctly inserted into the *Pgap4* allele were introduced to early embryos. The obtained chimeric mice were then crossed with wildtype (WT) mice to obtain heterozygous PGAP4-KO mice. Heterozygotes were crossed with each other, and the genotypes of the obtained mice were determined by PCR (Fig. 1*C*). PGAP4-KO mice were viable and born along with Mendel's laws (41:98:54), and both male and female KO mice were fertile, indicating that PGAP4 is not essential for embryonic development and fertilization. Quantitative reverse transcriptional PCR using various tissue samples was performed to reveal the tissue distribution of *Pgap4* mRNA. We found that *Pgap4* expression was limited to specific tissues, including brain, lung, heart, kidney, and testis, with the highest expression in brain (Fig. 1*D*), whereas GPI-APs are expressed ubiquitously (3). This observation suggests that the GalNAc side chain may have specific functions in select tissues. In the brain, expression of PGAP4, which can be monitored by GFP expression in KO mice, was widely observed (Fig. S1*A*). Costaining of hippocampal sections for GFP and markers for neurons (NeuN), astrocytes (GFAP), and microglia (Iba1) showed that PGAP4 is expressed predominantly in neurons (Figs. 1*E* and S1, *B* and *C*).

Loss of the GPI-GalNAc side chain in PGAP4-KO mice

The *in vivo* functions of the GalNAc side chain were examined by first investigating protein expression of particular GPI-APs in the brain. The expression levels of three GPI-APs, NCAM120 (NCAM has three transcriptional isoforms, NCAM180, NCAM140, and NCAM120, in which NCAM120 is the only GPI-AP), PrP^C, and Thy1 in KO mouse brains were comparable with those in WT brains (Fig. 1*F*). This result indicates that the GalNAc side chain is dispensable for the expression of these GPI-APs in cells. Next, we investigated whether adding the GalNAc side chain contributes to the association of GPI-APs with lipid rafts. To this end, we treated the brain homogenates with cold detergent (Triton X-100) and isolated the undissolved fraction as DRM. All three GPI-APs, NCAM120, PrP^C, and Thy1, were detected primarily in the DRM fraction and the detection levels were similar between WT and KO samples (Fig. 1*G*), indicating that the GalNAc side chain does not contribute to raft association of GPI-APs.

We noticed that mobility in SDS-PAGE of PrP^C and Thy1 from KO brain was slightly faster than WT proteins (Fig. 1, *F* and *G*), suggesting that glycosylation of these proteins was altered in KO mice. To investigate whether the mobility shift of these proteins is due to an alteration of *N*-glycan structures, we treated the brain samples with or without peptide-*N*-glycosidase F (PNGase F) to remove *N*-glycans. Even after PNGase F treatment, the mobility difference between WT and KO samples was still observed (Fig. 1*H*, compare lanes 3 and 4), strongly suggesting that GPI structures, but not *N*-glycans on these proteins, are altered in KO mice. We purified PrP^C from brain membrane lysates to determine the precise GPI structures in the KO mouse brain (Fig. S2*A*) and removed *N*-glycans and GPI-lipids by treatment with PNGase F and

phosphatidylinositol-specific phospholipase C (PI-PLC), respectively. Peptides were obtained by in-gel digestion. Liquid chromatography-mass spectrometry (LC-MS) analysis using a C18 column identified peptides mainly from PrP^C (Table S1). We then analyzed the structures of GPI-glycans by LC-MS using a HILIC column (Fig. S2, *B* and *C*). We identified two species of GPI-glycans in WT PrP^C, Hex-HexNAc-(Hex)GPI, and HexNAc-(Hex)GPI; both contain the GalNAc side chain (Fig. 1*L* and Table S2). Contrary to our expectation based on previous structural analysis of hamster and human PrP^C GPIs (6, 7), we did not find GPI with sialic acid. This observation was most likely because the amount of WT PrP^C we obtained and used for mass spectrometry (MS) analysis was too small. In contrast to PrP^C from WT brains, (Hex)GPI and GPI only, neither of which has the GalNAc side chain, were detected in PrP^C from KO brains (Fig. 1*I* and Table S2). This demonstrated that loss of PGAP4 almost completely abolished the presence of the GalNAc side chain in the brain.

The presence of Hex-HexNAc-(Hex)GPI in WT but not in KO PrP^C strongly suggests that the GalNAc side chain is elongated with a Gal residue in WT brain. To confirm that PGAP4 and B3GALT4, the GalNAc and Gal transferases, respectively, are expressed in the same cells, we simultaneously detected GFP and *B3galt4* mRNA by immunohistochemistry and *in situ* hybridization, respectively. In all three brain regions (cerebral cortex, hippocampus, and cerebellum) tested, *B3galt4* signals overlapped well with GFP signals in the KO mouse sections (Fig. 1*J*, white arrowhead), whereas cells with PGAP4 expression without *B3galt4* expression were hardly detected (Fig. 1*J*). These results indicated that PGAP4 and B3GALT4 are expressed in the same cells and the GalNAc side chain is elongated by Gal in the brain.

To further investigate the role of PGAP4 in adding GalNAc to GPI *in vivo*, we examined the production of GalNAc-modified free GPI (Fig. 1*A*, right), that is, the protein-unlinked form, and detected this species with the specific antibody termed T5_4E10 (T5) (8, 43). T5 mAb recognizes free GPI when it has the GalNAc side chain but only when the GalNAc is at the nonreducing end. In Western blotting of the medulla oblongata, where GalNAc-modified free GPI was reported to be highly expressed (43), we detected a strong T5 signal in heterozygous mice, whereas the signal was noticeably reduced in KO (Fig. 1*K*). Immunofluorescence staining also detected T5 signals in WT pyramidal neurons in the CA3 region of the hippocampus (in which PGAP4 was expressed, as shown in Fig. 1*E*), whereas the signals were essentially absent in the KO mouse section (Fig. 1*L*). Taken together, we concluded that PGAP4 is the major GalNAc transferase for the GPI-anchor of both GPI-APs and free GPI in the brain and loss of the GPI-GalNAc side chain does not influence the expression and raft association of GPI-APs.

Abnormal bone formation in PGAP4-KO mice

To investigate the *in vivo* functions of PGAP4, a biochemical blood test was first performed. This testing revealed that most of the contents including lactate dehydrogenase, aspartate aminotransferase, albumin, uric acid, creatinine, glucose,

total bilirubin, low-density lipoprotein cholesterol, and triglyceride were unaltered in KO mice (Table S3), indicating that the liver and kidney functions and metabolisms of glucose and lipids were normal. This set of results was supported by urinalysis, in which all contents were normal in KO mice (Table S3). Surprisingly, the level of blood ALP was noticeably increased (about three times that of WT) in KO mice (Fig. 2A, left), implying that the cell surface level of ALP is decreased in KO mice. Moreover, the blood calcium level was also significantly increased in KO mice (Fig. 2A, right). These results suggested that bone calcification decreases in KO mice because ALP is required for calcification of bones (44–46). As expected, mineral content and area of bone were both lower in KO mice (Fig. 2B and Table S3). We also investigated the formation of the skeletal frame by X-ray analysis. Although there was no difference in the shapes of most skeletal bones, including clavicle, femur, and humerus in KO mice (Table S3), abnormal shapes of rib and vertebrae were frequently observed (Fig. 2, C and D). Furthermore, the tibia length in KO mice was shorter than that in WT mice (Fig. 2E). These results indicated that the GPI-GalNAc side chain is required for normal bone formation.

We also performed hematological, body composition, funduscopy, electrocardiogram, and immunophenotyping tests (Table S3). Although PGAP4-KO mice showed similar results to WT in most tests, several phenotypes were observed. For example, the electrocardiogram results showed that mean R amplitude increased slightly in PGAP4-KO mice (Table S3), suggesting the left ventricle was enlarged in KO mice. Among immune cells, the NK cell population changed slightly in KO mice, with increases and decreases in CD11b$^-$ and CD11b$^+$ cell populations observed, respectively (Table S3), thus suggesting the altered differentiation of NK cell types in KO mice.

Reduced locomotion activity and impaired memory formation in PGAP4-KO mice

Based on the high expression of *Pgap4* in the brain, we next asked whether PGAP4 is required for brain functions and performed various behavioral tests. In the open field test, the distance traveled by KO mice decreased, especially in the periphery of the field (Figs. 3A and S3A, upper), and the average speeds were also significantly reduced (Fig. S3A, middle). These results indicated that PGAP4-KO mice have reduced locomotion activity. The percentages of center time and latency to center entry were unchanged between WT and KO mice (Fig. S3A, lower), suggesting that anxiety-like behavior was not observed. The home cage activity test also showed that activity decreased in KO mice when compared with that of WT mice (Fig. 3, B and C). These findings suggest that the GPI-GalNAc side chain is required for normal locomotor activity.

We next conducted a sociability test. KO mice spent more time near a low stimulating object when compared with the time spent by WT mice (Fig. 3D, left). In contrast, when a stranger mouse was included, there was no difference in time spent near the stranger mouse between WT and KO mice (Fig. 3D, right), indicating that loss of the GPI-GalNAc side chain enhances interest in novel objects but not to strangers. We also performed a pre-pulse inhibition test and found no difference in the response to the test pulse between WT and
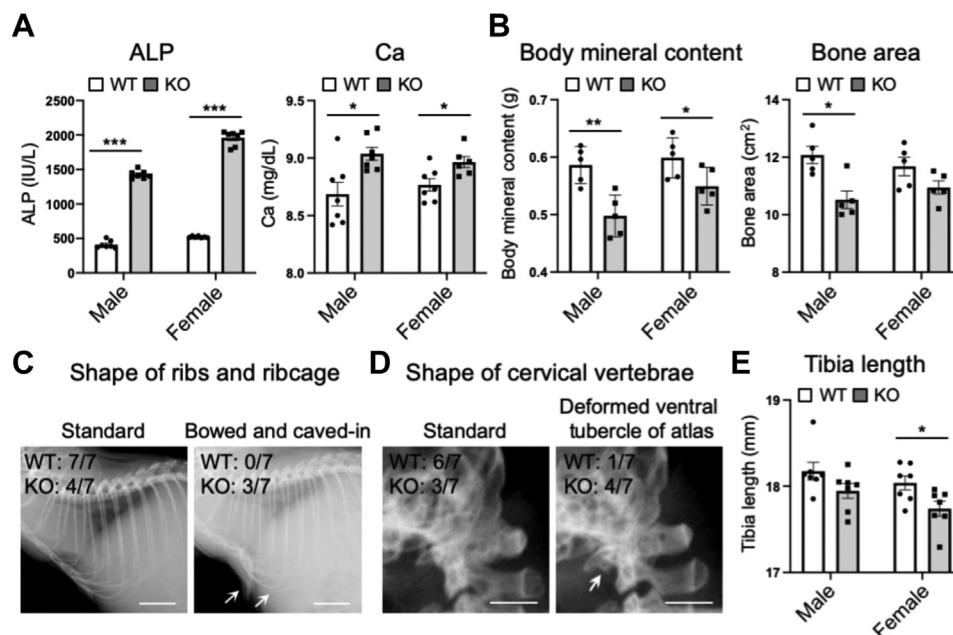

Figure 2. Abnormal bone formation in PGAP4-KO mice. *A*, blood alkaline phosphatase level (ALP) and blood calcium level (Ca) are shown. Error bars represent SEM ($n = 7$). Statistics was calculated by Welch's *t* test (ALP) and unpaired Student's *t* test (Ca). *B*, body mineral content and bone area are shown. Error bars represent SEM ($n = 5$). Statistics was calculated by unpaired Student's *t* test. *C*, the representative images of normal and abnormal shapes of ribs and ribcage. The number of male mice showing the phenotypes is indicated. The scale bar represents 5 mm. *D*, the representative images of normal and abnormal shapes of cervical vertebrae. The number of female mice showing the phenotypes is indicated. The scale bar represents 2 mm. *E*, Tibia length is shown. Error bars represent SEM ($n = 7$). Statistics was calculated by unpaired Student's *t* test. *p < 0.05; **p < 0.005; ***p < 0.0005.
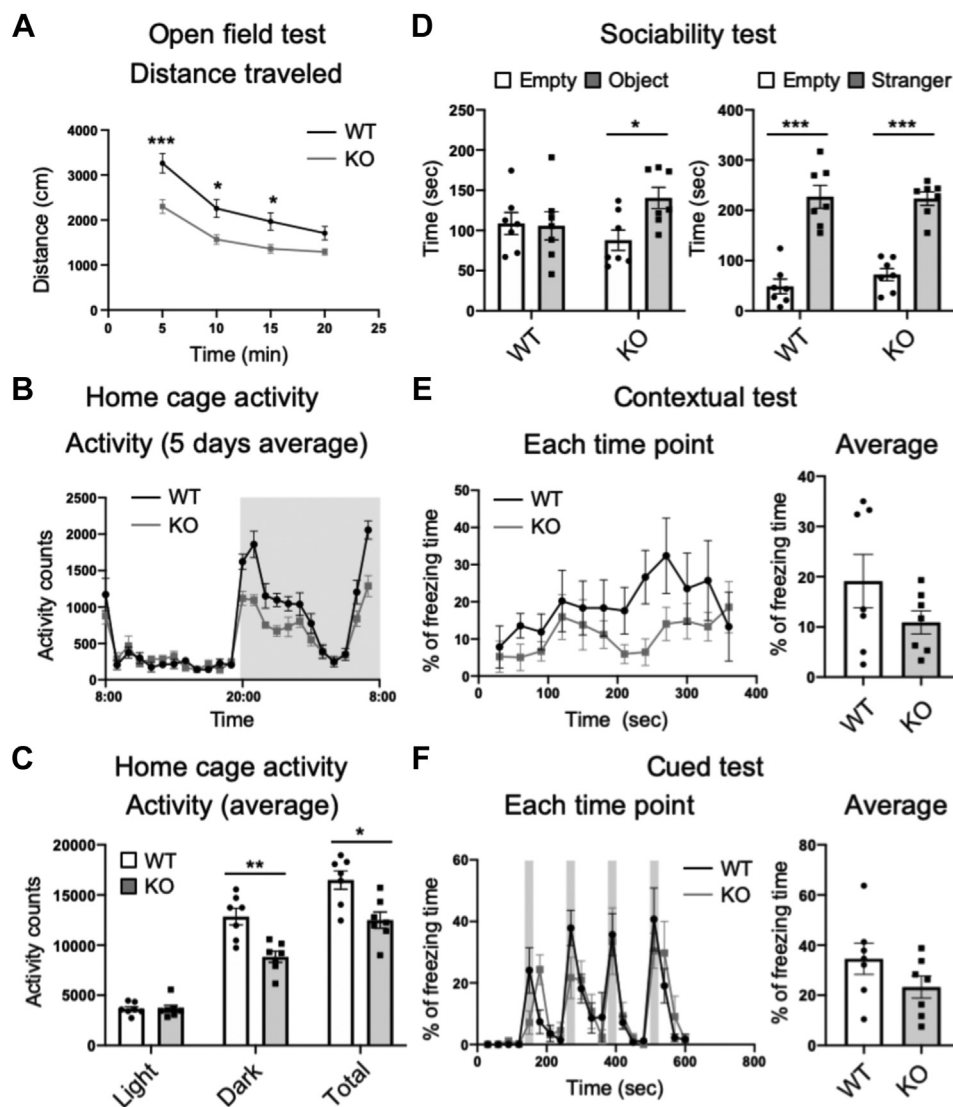
Figure 3. Reduced locomotion activity and impaired memory formation in PGAP4-KO mice. *A*, the graph indicates the distance traveled for each 5 min in open field test. Error bars represent SEM ($n = 7$). Statistics was calculated by two-way ANOVA post hoc Sidak test. *B*, home cage activity test for 24 h was performed. The average activity score for 5 days is shown. The *gray area* indicates the dark state. *C*, the graph indicates activity in light (*Light*), activity in dark (*Dark*), and total activity (Total) in home cage activity test. Error bars represent SEM ($n = 7$). Statistics was calculated by unpaired Student's *t* test. *D*, sociability test was performed. Times that mice spent in front of the cage with an unstimulating novel object (*left*) or a stranger mouse (*right*) are shown. Error bars represent SEM ($n = 7$). Statistics was calculated by two-way ANOVA post hoc Sidak test. *E*, contextual test was performed. *Left*, percentage of freezing time at each time point is shown. *Right*, the average percentage of freezing time is shown. Error bars represent SEM ($n = 7$). Statistics was calculated by unpaired Student's *t* test. *F*, cued test was performed. *Left*, percentage of freezing time at each time point is shown. *Right*, the average percentage of freezing time is shown. *Gray areas* indicate the timing of test tone. Error bars represent SEM ($n = 7$). Statistics was calculated by unpaired Student's *t* test. *$p < 0.05$; **$p < 0.005$; ***$p < 0.0005$.

KO mice (Fig. S3*B*), indicating that PGAP4-KO mice do not show a schizophrenia-like phenotype.

We next examined whether loss of the GPI-GalNAc side chain affects memory formation by contextual and cued fear conditioning tests, in which amygdala and hippocampus, or amygdala are related to memory formation (47). Before tests, mice were trained with an electric pulse accompanied with a test sound in the test cage. In the contextual test on the following day, mice were placed in the same test cage without the electric pulse and the freezing time was measured. We found that KO mice showed shorter freezing time throughout the experiments (Fig. 3*E*, left) and the average freezing time of KO mice was lower when compared with that of WT, although the difference was not statistically significant (Fig. 3*E*, right), suggesting that KO

mice have impaired memory formation. In the cued test, mice were placed in the other cage the day after the contextual test and stimulated with the test sound without the electric pulse and freezing time was measured. Although the difference was not statistically significant, the freezing time of KO mice was shorter when compared with that of WT mice (Fig. 3*F*). These results suggested that loss of the GPI-GalNAc side chain impaired memory formation especially in hippocampus.

Histology and expression of marker proteins in PGAP4-KO mouse brain

Having discovered impaired brain functions in PGAP4-KO mice, we next examined the histology of PGAP4-KO mouse brains. Hematoxylin and eosin staining of five brain regions,

cortex, hippocampus, thalamus, cerebellum, and medulla oblongata, showed no apparent abnormality in PGAP4-KO mouse brains (Fig. 4, *A* and *B*), demonstrating that the GPI-GalNAc side chain is dispensable for cell viability and brain development.

We next investigated the expression levels of marker proteins for brain cell types: microtubule-associated protein 2 (MAP2) and postsynaptic density protein 95 (PSD95) for neurons, myelin associated glycoprotein (MAG) and myelin basic protein (MBP) for oligodendrocytes, ionized calcium-binding adaptor molecule 1 (Iba1) for microglia, and glial fibrillary acidic protein (GFAP) and aldehyde dehydrogenase family 1 member L1 (ALDH1L1) for astrocytes. The expression levels of these neuronal, oligodendroglial, and microglial markers in KO mice were comparable with those in WT mice (Fig. 4, *C* and *D*), suggesting the numbers of neurons, oligodendrocytes, and microglia did not differ in KO mice. Of note, the expression level of the astrocyte marker GFAP increased in KO mice, whereas no significant change in the expression level of ALDH1L1 was observed (Fig. 4, *C* and *D*). As expression of GFAP but not ALDH1L1 increases during brain inflammation (48), this result suggests that loss of the GPI-GalNAc side chain does not alter the number of astrocytes but likely causes activation of astrocytes.

Enhanced progression of the pathology of prion diseases in PGAP4-KO mice

Finally, we examined the pathological roles of the GPI-GalNAc side chain. Previous studies reported that desialylation of PrP^C GPI caused a delay of PrP^{Sc} production (39, 40). Considering that sialic acid in GPI was solely found on the GalNAc side chain, it is possible that the GalNAc side chain is involved in progression of prion diseases. Therefore, we examined whether loss of GalNAc modification impacts the lifespan of PrP^{Sc} inoculated mice. We used two PrP^{Sc} strains, Fukuoka-1 (a mouse-adapted GSS syndrome prion strain) (49) and Chandler (a mouse-adapted scrapie prion strain) (50). Both WT and KO mice were intracerebrally inoculated with PrP^{Sc} strains, and their lifespan was examined. We found that KO mice showed significantly shorter incubation period after inoculation with both types of PrP^{Sc} strains (Fig. 5, *A* and *B*). However, the accumulation of PrP^{Sc} in deceased KO mouse brains was comparable with that in WT mice, as assessed by Western blotting and immunohistochemistry (Fig. 5, *C* and *D*). Similarly, GFAP and Iba1 signals in the inoculated KO mouse brains were comparable with those in the inoculated WT brains (Fig. 5*D*), indicating that gliosis levels were similar. These results suggested that propagation of PrP^{Sc} but not its toxicity is increased in PGAP4-KO mouse brains. To directly investigate whether the conversion was accelerated, we performed inoculation experiments using Fukuoka-1 PrP^{Sc} strain and analyzed the amount of PrP^{Sc} at an early stage of incubation period (50 days post inoculation [dpi]). We found that accumulation of PrP^{Sc} was robustly enhanced in PGAP4-KO mice compared with WT mice (Fig. 5*E*), indicating that loss of the GPI-GalNAc side chain accelerated the conversion of PrP^C to PrP^{Sc}.

Discussion

In this report, we examined the *in vivo* roles of the GPI-GalNAc side chain by analyzing KO mice for its initiation enzyme, PGAP4. In contrast to the ubiquitous expression of GPI (3), *Pgap4* mRNA was expressed in specific tissues, including the brain, testis, lung, heart, and kidney (Fig. 1*D*). Consistent with this, GPI-APs purified from brain, kidney, and skeletal muscle were reported to be modified with the GalNAc side chain (5, 7, 51, 52). The tissue-specific expression of PGAP4 suggests that the GPI-GalNAc side chain regulates certain specific but nonessential functions of GPI. Loss of the GPI-GalNAc side chain does not influence the expression and DRM association of GPI-APs in the brain (Fig. 1, *E* and *F*) and cultured cells (8) but causes abnormality in several tissues, particularly in bone and brain. Therefore, the present work demonstrated that the core GPI structure is not sufficient and the GalNAc side chain is also required for the full activity of some GPI-APs in mammals. To fully understand the function of the GPI-GalNAc side chain, it is important to elucidate how this side chain regulates folding, localization, and protein–protein interactions of GPI-APs.

The phenotypes observed in PGAP4-KO mice, including elevated blood ALP levels, abnormal bone formation, lowered locomotion activity, and impaired memory, are also reported for patients with IGD (21). Nevertheless, *PGAP4* has not been identified previously as a responsible gene of IGD. The current diagnosis of IGD largely depends on the exome sequencing of patients who have severe epilepsy and intellectual disability, whereas PGAP4-KO mice never naturally showed epileptic symptoms, raising the possibility that patients with *PGAP4* mutations may be undiagnosed. In the future, patients with *PGAP4* mutations might be found who show elevated blood ALP levels (hyperphosphatasia), abnormal bone morphology, or mild intellectual disabilities without epileptic symptoms.

The blood level of ALP, a GPI-AP expressed on the cell surface, was highly elevated in PGAP4-KO mice (Fig. 2*A*). Cell association of ALP may be impaired by loss of the GalNAc side chains from their GPIs, resulting in the liberation of ALP into blood plasma. Similarly, PGAP3-KO mice, in which GPI-lipid remodeling is impaired (17, 53), also showed elevation of the blood ALP level (17), and a similar phenomenon was also observed in patients with IGD harboring a *PGAP3* mutation (54). Therefore, structures of GPI critically regulate the cellular and secreted ALP levels *in vivo*. For some patients with IGD, it is suggested that aberrant activation of the GPI transamidase complex in the ER accelerates the cleavage of the GPI attachment signal peptide of ALP to produce its soluble secreted form (55). Because PGAP4 acts in the Golgi apparatus (8), however, loss of the GalNAc side chain likely promotes secretion of ALP by a different mechanism. Thus, it is important to examine whether there are other GPI-APs whose secretion is also promoted by PGAP4 depletion.

In association with elevated ALP and high Ca in the blood (Fig. 2*A*), bone mineral content and area of bone were lower in PGAP4-KO mice, and abnormal shapes of rib and vertebrae were frequently observed in PGAP4-KO mice (Fig. 2, *B–D*). Because ALP is critical for proper generation of hydroxyapatite
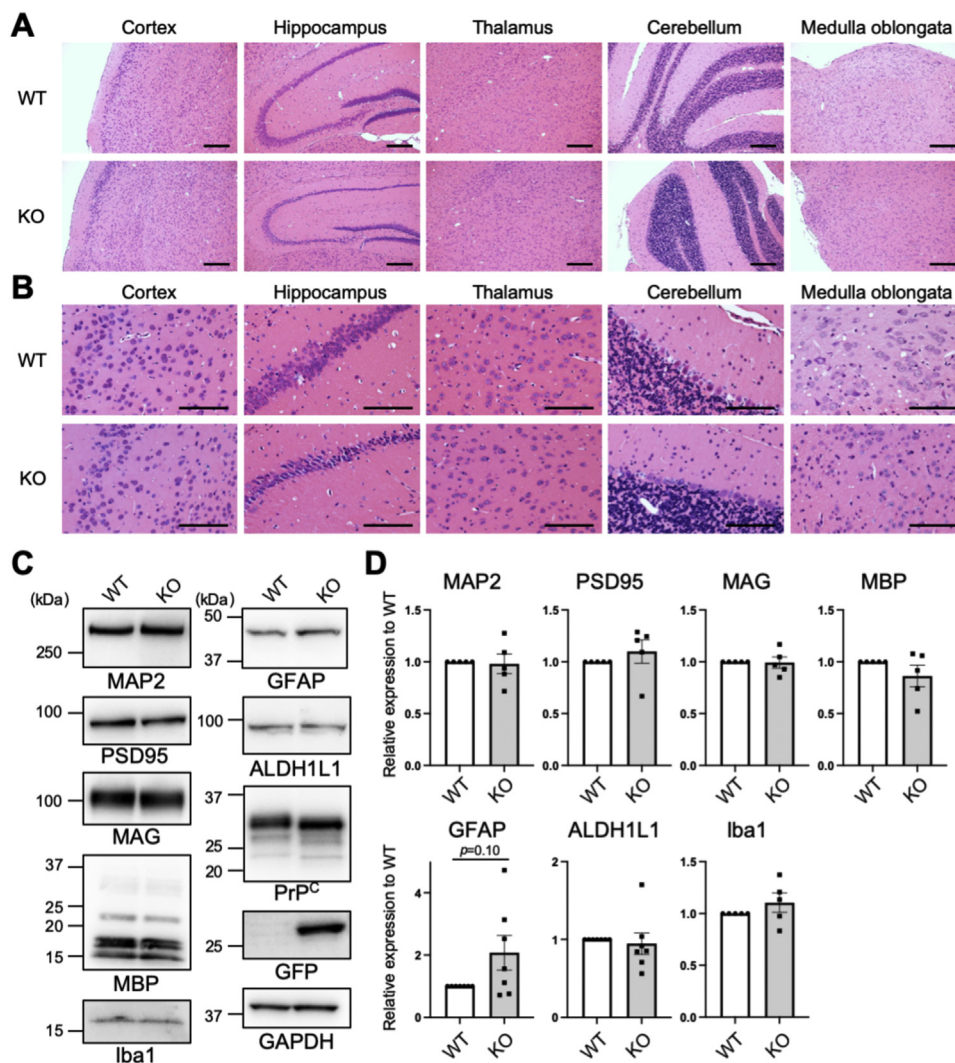
Figure 4. Histology and marker protein expression in PGAP4-KO mouse brain. *A*, coronal brain sections were stained with hematoxylin and eosin. Images of cerebral cortex, hippocampus, thalamus, cerebellum, and medulla oblongata are shown. The scale bar represents 200 μm. *B*, magnified images shown in *A*. The scale bar represents 100 μm. *C*, brain lysates from WT and PGAP4-KO mice were blotted for MAP2 and PSD95 (neuronal marker), MAG and MBP (oligodendrocytic marker), Iba1 (microglial marker), GFAP and ALDH1L1 (astrocytic marker), PrP^C, GFP, and GAPDH. *D*, the graphs show quantification of each marker protein signals in Western blotting shown in *C*. Error bars represent SD ($n = 5$, for GFAP and ALDH1L1 $n = 7$). Statistics was calculated by Welch's *t* test.

in the bone through the regulation of pyrophosphate levels (45), it seems that impaired membrane association of ALP in PGAP4-KO mice might be the basis of these bone abnormalities.

We noticed that some phenotypes, such as high body fat percentage and fat mass in male PGAP4-KO mice, were detected in sex-dependent manners (Table S3). Although the mechanisms for this sex dependency remain unclear, the similar sex-dependent differences were observed in various phenotypes in a large-scale analysis (56).

PGAP4-KO mice exhibited various behavioral impairments, such as lowered locomotion activity, increased interest in an unknown object, and impaired memory. Interestingly, despite the reduced locomotion activity of KO mice in the dark state, the activity of these mice in the light state was similar to that of WT mice (Fig. 3, *B* and *C*). This result indicates that the lowered locomotion activity of KO mice may not be because of motor ataxia, which is observed in patients with IGD (21) and

phosphatidylinositol-glycan biosynthesis class A protein (PIGA)-KO mice (18), but likely because of psychological illness. There are many GPI-APs in the brain, including the immunoglobulin superfamily of cell adhesion molecules (including contactins, NCAM120, and Thy1), PrP^C, folate receptors, ephrin A family members, and glypicans (3, 57). These proteins are involved in neurite outgrowth, axonal guidance, and synaptic formation (58–62), and loss of GPI-APs impairs synaptic transmission and reduces long-term potentiation in the hippocampus (19, 57, 63). Therefore, the dysfunction of one or more of those GPI-APs may cause the behavioral phenotypes in PGAP4-KO mice. As no GPI structures of those GPI-APs except for Thy1 and PrP^C have been determined, it is important to determine their GPI structures, which should facilitate our understanding of the cause of dysregulated brain functions in PGAP4-KO mice.

PGAP4-KO mice showed a shorter incubation period of prion diseases than WT mice (Fig. 5). This observation can be
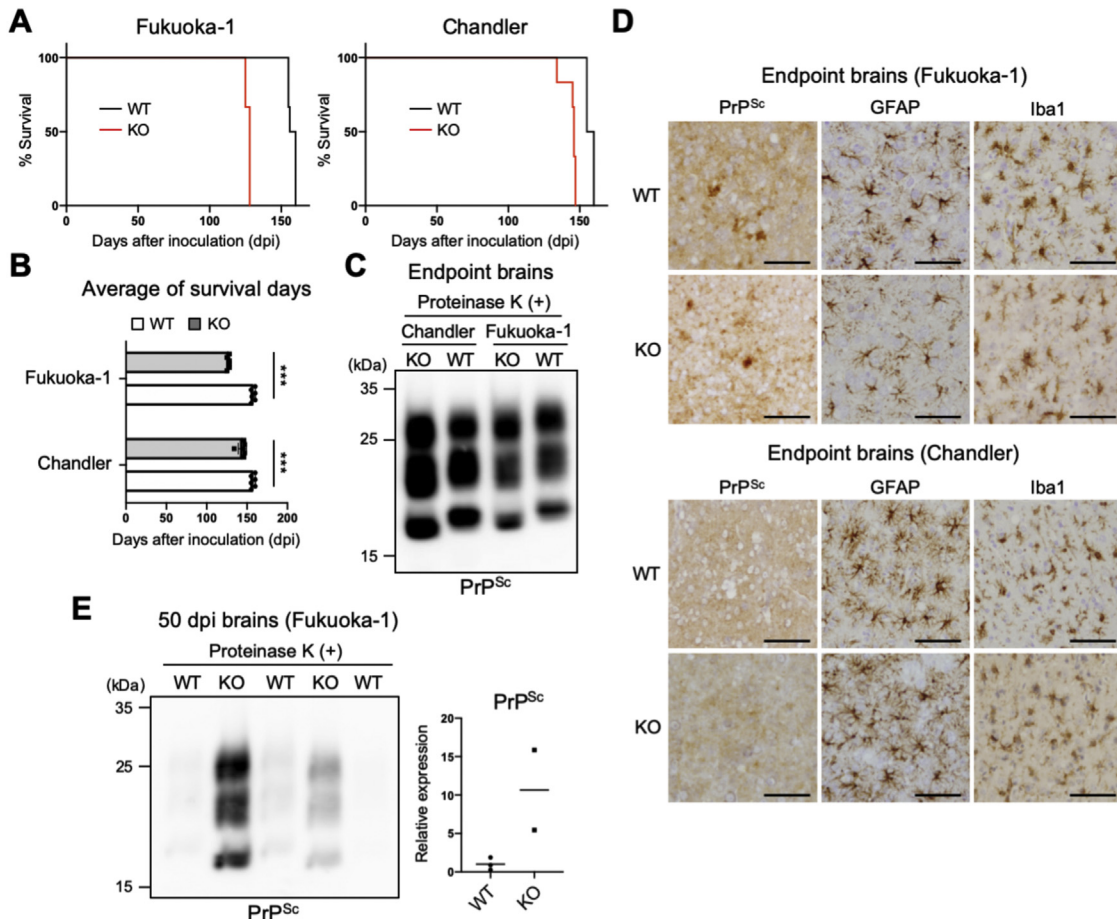
Figure 5. Enhanced progression of the pathology of prion diseases in PGAP4-KO mice. *A*, survival curve of WT and PGAP4-KO mice after intracerebral inoculation of PrP^{Sc} strains (Fukuoka-1 [*left*] and Chandler [*right*]) are shown ($n = 6$). *B*, average survival days of WT and PGAP4-KO mice after inoculation of PrP^{Sc} strains (Fukuoka-1 and Chandler) are shown. Error bars represent SD ($n = 6$). Statistics was calculated by two-way ANOVA post hoc Sidak test. *C*, brain lysates from WT and PGAP4-KO mice inoculated with PrP^{Sc} strains were treated with proteinase K and were blotted for PrP^{Sc}. *D*, the coronal brain sections were stained for PrP^{Sc}, GFAP (astrocyte), and Iba1 (microglia). The scale bar represents 100 µm. *E*, brain lysates at 50 dpi from WT and PGAP4-KO mice inoculated with Fukuoka-1 PrP^{Sc} strain were treated with proteinase K and were blotted for PrP^{Sc}. The graph showed the relative band intensities of PrP^{Sc} in PGAP4-KO mice to WT mice. Bars indicate the mean ($n = 3$ for WT, $n = 2$ for KO). *** $p < 0.0005$.

explained by either or both enhanced toxicity of PrP^{Sc} or rapid conversion of PrP^{C} to PrP^{Sc} in PGAP4-KO mice. Because the activation of astrocytes from a neuroprotective type to an inflammatory type was reported to enhance PrP^{Sc} toxicity (64), the aberrant activation of astrocytes may cause a shorter incubation period in PGAP4-KO mice, as shown by the elevated GFAP expression (Fig. 4). However, given that the accumulation of PrP^{Sc}-, GFAP-, and Iba1-positive cells at endpoints in PGAP4-KO mice was comparable with that in WT mice (Fig. 5, *C* and *D*), enhancing the intrinsic toxicity of PrP^{Sc} in KO mice is unlikely. In addition, more aggressive types of PrP^{Sc} might be produced in PGAP4-KO mice, but more rigorous experiments will be required to obtain conclusive evidence regarding aggressiveness. Instead, considering the enhanced accumulation of PrP^{Sc} in PGAP4-KO mice (Fig. 5*E*), we hypothesized that the conversion process is directly altered in PGAP4-KO mice. This was also supported by the previous report that sialylation of GPI, which has been identified only on the GalNAc side chain, regulates the conversion of PrP^{C} to PrP^{Sc} (39). As to the mechanisms of how the GPI-GalNAc side chain of PrP^{C} influences the conversion to PrP^{Sc}, one

possibility is that the GalNAc side chain regulates localization (including nanoscale compartmentalization or clustering) of PrP^{C}, as suggested by a previous report (40). Alternatively, the GPI-GalNAc side chain may affect the folding status of PrP^{C} as glycosylation generally contributes to protein folding (65). Detailed microscopic and structural studies of GPI-anchored PrP^{C} are required to elucidate these points.

In our present LC-MS analysis, the sialylated form of the side chain was not detected in PrP^{C} from WT mouse brain (Table S2). Therefore, combined with a previous report (40), it is suggested that asialo forms of GPI-GalNAc side chain (Gal-GalNAc-GPI and GalNAc-GPI) have protective function from prion diseases. Because human PrP^{C} GPI is more likely to be sialylated (approximately 40% in human brain (7)) than mouse PrP^{C} GPI, augmented desialylation on the GPI-GalNAc side chain may be an effective novel therapeutic for treating human prion diseases. Elucidation of the relationship between structure and function of the GPI-GalNAc side chain will facilitate our understanding of the pathology of prion diseases and the development of therapeutics based on the structure of the GPI-GalNAc side chain.

Pathophysiology of GPI-GalNAc side chain

In summary, we have investigated the *in vivo* functions of the GPI-GalNAc side chain and found that this side chain is required for bone formation and brain functions and plays a protective role against prion diseases. These results demonstrate that the GPI-GalNAc side chain is indispensable for our health and manipulation of the structures of the GPI-GalNAc side chain may lead to the development of therapeutics for treating prion diseases. It is crucial to clarify the mechanisms of how the GPI-GalNAc side chain regulates the functions of GPI-APs and how the biosynthesis of the GPI-GalNAc side chain is regulated *in vivo*.

Experimental procedures

Ethics statement

Animal experiments were performed in strict accordance with the Regulations for Animal Experiments and Related Activities at Gifu University, Hokkaido University, and Osaka University, and Fundamental Guidelines for Proper Conduct of Animal Experiment and Related Activities in Academic Research Institutions by the Ministry of Education, Culture, Sports, Science, and Technology in Japan, Notice 71. The protocol was approved by the Institutional Animal Care and Use Committee of Gifu University, Hokkaido University, and Osaka University (2020-235, 14-0170, Biken-AP-H28-02-0).

Animals

Eight- to ten-week-old littermate animals were used for biochemical and histological analyses throughout the study. For phenotype analyses, age-matched male and female mice were used. All these analyses were done in RIKEN BioResource Research Center. For PrP^{Sc} inoculation experiments, 4- to 7-week-old mice were intracerebrally inoculated with indicated prion strains and the inoculated mice were sacrificed at a predefined clinical endpoint or at the time point showing intercurrent illness.

Plasmid construction

To construct a Cas9 expression plasmid harboring gRNA targeting to mouse *Pgap4* (*Tmem246*) gene, pX459 v2.0 plasmid (Addgene, #62988), which is a gift from Feng Zhang (66) was cut by BbsI, followed by ligation with annealed primer. The sequence of the primer was 5′- AGGCTTCGG CGACTCTCCTG-3′.

To construct a knock-in vector, homology arms were amplified by PCR using mouse genome as a template with following primer sets: mPgap4-KI-EcoRI-F1 and mPgap4-KI-MluI-R1 (5′-AAAAgaattcATTCGACCAGCAGGCTAAG-3′ and 5′-AAAAacgcgtAAGCCTCCGGAGAAGCAT-3′) and mP gap4-KI-NotI-F2 and mPgap4-KI-SpeI-R2 (5′-AAAAgcggccgc CACAGCTGTGCAGCTCTTC-3′ and 5′-AAAAactagtGTAC CGTAGGCTGGAGAAGAG-3′). Monomeric EGFP (mEGFP) sequence was obtained by clipping from pME-mEGFP plasmid with MluI and NotI. The knock-in vector was obtained by ligation with the two homology arms and mEGFP sequence into pBlueScript II (+) vector cut by EcoRI and SpeI.

Generation of PGAP4-KO mice

PGAP4-KO mice (C57BL/6-Tmem246<em1(EGFP)Osbir> mice) were generated by transfection of pX459 plasmid into C57BL/6-derived embryonic stem (ES) cells (EGR-G101 (67)) as described (68). For EGFP knock-in, the knock-in vector was cotransfected into the ES cells together with pX459 plasmid targeting to mouse *Pgap4* gene. Screening of the ES cells in which *EGFP* sequence was successfully knocked in was performed by amplification of inserted regions by PCR followed by direct sequencing. The primer sets used were as follows: ES-F1 and ES-R1 (5′-GTCTAGGATCTCTGCACTGGC-3′ and 5′-AACAGCTCCTCGCCCTTG-3′) and ES-F2 and ES-R2 (5′-TAAGGAGTTCGTGACCGCC-3′ and 5′-GAATCCAGTGT GTGCCTCTCC-3′). The mutant ES cells were injected into eight-cell-stage ICR embryos, and the embryos were transferred into the uterus of pseudopregnant ICR females the next day. Genotyping of the obtained mice was performed by PCR using the following primer sets: F1, R1, and R2 (5′-CTTCTG ATTCGGTGTGTGCTG-3′, 5′-GGAAGTCCTGGCTCATCT GG-3′, and 5′-AACAGCTCCTCGCCCTTG-3′, respectively).

Antibodies and reagents

The following antibodies were obtained and used: mouse IgM mAb against *Toxoplasma gondii* free GPI (clone T5_4E10, T5 antibody) (a gift from Dr Jean François Dubremetz (Montpellier University, France), available from the BEI Resources, NIAID, NIH (69, 70); rabbit anti-PrP^C (termed ChW) (a gift from Dr Tetsuyuki Kitamoto, Tohoku University, Japan) (71); anti-GAPDH mAb (clone 6C5), rat anti-MBP mAb (clone 82-87), and anti-ALDH1L1 (clone N103/39) from Millipore (MAB374, MAB386, and MABN495); anti-α-tubulin (clone DM1A), from Sigma-Aldrich (T9026); rabbit anti-NCAM, rabbit anti-PrP mAb (clone EP1802Y), rabbit anti-Thy1 (clone G7), rabbit anti-GFP mAb (clone EPR14104-89), anti-NeuN mAb (clone 1B7), and goat anti-Iba1, from Abcam (ab220360, ab52604, ab95701, ab183735, ab104224, and ab5076); rabbit anti-GFP, from MBL (598); rabbit anti-MAP2, from Santa Cruz (sc-20172); anti-PSD95 (clone 7E5); rabbit anti-MAG, from Cell Signaling Technology (#36233 and #9043); rabbit anti-Iba1, from FUJIFILM Wako (019-19741); rat anti-GFAP (clone 2.2B10), from ThermoFisher Scientific (13-0300); rabbit anti-GFAP, from Dako (Z0334); horse radish peroxidase (HRP)-conjugated anti-mouse IgG and HRP-conjugated anti-rabbit IgG from GE Healthcare (NA931V and NA934V); HRP-conjugated anti-mouse IgM, Alexa488-conjugated anti-rabbit IgG, Alexa546-conjugated anti-mouse IgG, Alexa546-conjugated anti-rat IgG, and Alexa546-conjugated anti-mouse IgM from ThermoFisher Scientific (31440, A21206, A10036, A11081, and A21045).

The following kits and reagents were purchased and used: RNeasy mini kit and RNase-free DNase set (DNase I) (Qiagen, 74104 and 79254); TaqMan Gene Expression Master Mix (Applied Biosystems, 4369016); Peptide-N-glycosidase F (Roche, 11365169001 and New England Biolabs, P0704); PI-PLC (ThermoFisher Scientific, P6466).

RNA extraction, reverse transcription, and real-time PCR

The total RNA was extracted from WT mouse tissues with TRI Reagent (Molecular Research Center) by homogenizing using Potter homogenizer. The extracted RNA was treated with DNase I (Qiagen) and purified with RNeasy mini kit (Qiagen) according to manufacturer's protocol. One microgram of purified total RNA was reverse transcribed using the SuperScript IV First-Strand Synthesis System (ThermoFisher Scientific) with random hexamer (supplied in the kit). The target cDNAs were amplified using a TaqMan Gene Expression Master Mix (Applied Biosystems) and the primers and probes described below. The amplified cDNAs were detected using a CFX Connect Real-Time PCR Detection System (Bio-Rad). The primers and probes were purchased from Applied Biosystems as follows: Mm00727999_s1 for *Tmem246 (Pgap4)*. Ribosomal RNA (rRNA) was detected using Ribosomal RNA Control Reagents (VIC probe) purchased from Applied Biosystems (4308329). The mRNA levels of *Pgap4* were normalized to those of the rRNA levels.

Sample preparation for Western blotting

WT and PGAP4-KO mouse brains were homogenized in 20 mM Tris (pH 7.4) containing 150 mM NaCl and protease inhibitor cocktail using Potter homogenizer. The homogenates were centrifuged at 1000*g* for 10 min at 4 °C to remove cell debris and nuclei. The supernatants were collected and the protein concentrations were measured using BCA kit. For some experiments, membrane fractions were prepared by ultracentrifugation of the post-nuclear homogenates at 100,000*g* for 60 min at 4 °C, and the pellets were dissolved in the lysis buffer (50 mM Tris [pH 7.4], 150 mM NaCl, 1 mM EDTA, 60 mM Octyl-β-D-glucoside) containing protease inhibitor cocktail by sonication. The protein concentrations were measured using BCA kit. The samples were prepared by mixing with 5 × Laemmli's SDS sample buffer and incubated at 95 °C for 5 min. For detection of Thy1 protein, membrane fraction was used and mixed with 5 × Laemmli's SDS sample buffer without 2-mercaptethanol (2ME) and incubated at 95 °C for 5 min. The same protein amounts were loaded on SDS polyacrylamide gels.

For PNGase F treatment, the homogenates were denatured in denaturing buffer (20 mM Tris [pH 7.4], 0.5% SDS, 1% 2ME, 5 mM EDTA) at 95 °C for 5 min, followed by 5 times dilution with Tris-buffered saline (TBS) containing Nonidet P-40 (NP-40, final concentration, 0.5%). Sixty microliters of the samples were then incubated with 3 μl of water or PNGase F (Roche) at 37 °C for more than 2 h. The samples were then mixed with 5 × Laemmli's SDS sample buffer and incubated at 95 °C for 5 min. For detection of Thy1 protein, the membrane fractions were denatured in denaturing buffer without 2ME at 95 °C for 5 min, followed by the above-mentioned procedures. The samples were mixed with 5 × Laemmli's SDS sample buffer without 2ME and incubated at 95 °C for 5 min.

Western blotting

The same amount of protein was loaded in each well, and proteins were separated by SDS-PAGE followed by transfer to a nitrocellulose membrane or a PVDF membrane. Membranes were blocked with 5% skim milk in TBS containing 0.1% Tween-20 (TBS-T) for 30 min, followed by incubation with primary antibody diluted with 5% skim milk/TBS-T overnight at 4 °C. After washing with TBS-T three times, membranes were incubated with secondary antibody conjugated with HRP for 1 h at room temperature. Signals were detected using FUSION SOLO 7s EDGE (Vilber). Dilutions of antibodies were anti-NCAM (1:500); anti-PrP^C (from Abcam) (1:500); anti-Thy1 (1:500); anti-GFP (1:300); anti-GAPDH (1:2000); anti-PSD95 (1:500); anti-T5 (1:500); anti-α-tubulin (1:2000); anti-MAP2 (1:500); anti-MAG (1:500); anti-MBP (1:500); anti-Iba1 (1:500); anti-GFAP (1:500); anti-ALDH1L1 (1:1000); anti-mouse IgG-HRP (1:5000); anti-rabbit IgG-HRP (1:15,000); and anti-mouse IgM-HRP (1:2000).

Purification of PrP^C

WT and PGAP4-KO mouse brains (four brains for each genotype) were homogenized in 5 ml of 20 mM Tris (pH 7.4) containing 150 mM NaCl and protease inhibitor cocktail using Potter homogenizer. The homogenates were centrifuged at 1000*g* for 10 min at 4 °C to remove cell debris and nuclei. The supernatant was ultracentrifuged at 100,000*g* for 60 min at 4 °C, and the pellets were dissolved in 5 ml of lysis buffer (50 mM Tris [pH7.4], 150 mM NaCl, 1 mM EDTA, 60 mM Octyl-β-D-glucoside) containing protease inhibitor cocktail by sonication. The samples were treated with 4 units of PI-PLC (ThermoFisher Scientific) for 1 h at 37 °C. After that, samples were incubated with 15 μl of anti-Prion antibody (ChW) for 1 h at 4 °C, followed by further incubation with Protein-G-Dynabeads at 4 °C overnight. The beads were washed with the lysis buffer three times. The bound PrP^C was denatured and eluted from the beads by incubation with 1 × Glycoprotein Denaturing buffer (supplied with PNGase F, New England Biolabs) for 5 min at 95 °C. The supernatants were treated with 5 μl of PNGase F (New England Biolabs) in buffer containing 1 × GlycoBuffer 2 (supplied with PNGase F, New England Biolabs) and 1% NP-40 in 100 μl scale at 37 °C overnight. The samples were diluted with 400 μl of water and subjected to the concentration to about 30 μl with Amicon-Ultra filter units (cut-off 10 kDa, Millipore) by centrifugation at 14,000*g* for 15 min at 4 °C. Twenty-five microliters of samples was subjected to SDS-PAGE, and the gel was stained with GelCode Blue Safe Protein Stain Reagent (ThermoFisher Scientific). The bands corresponding to PrP^C were excised and used for LC-MS analysis.

LC-electrospray ionization-MS analysis of PrP^C

Determination of GPI structure of mouse PrP^C was performed as described (7). The bands corresponding to PrP^C were excised, reduced with 10 mM DTT, and alkylated with 55 mM iodoacetamide, followed by in-gel digestion with trypsin. The samples were subjected to LC-electrospray ionization-MS/MS analyses. To confirm the presence of PrP^C in the bands, MS analyses were first performed using hydrophobic column as described (7). The samples were

purified with Zip-Tipµ-C18 pipette tips (Millipore) and data were collected in positive ion mode on a nanoLC system (Advance, Michrom BioResources) using a C18 column (0.1 × 150 mm) coupled to an LTQ Orbitrap Velos mass spectrometer (ThermoFisher Scientific). The mass tolerance for precursor ions was ±10 ppm. The mass tolerance for fragment ions was ±0.8 Da. The threshold score/expectation value for accepting individual spectra was $p < 0.05$. Estimation of false discovery rate was not set. The mobile phase consisted of water containing 0.1% formic acid (solvent A) and aceto-nitrile (solvent B). Peptides were eluted by a gradient of 5% to 35% solvent B over 45 min. The mass scanning range was set at m/z 350 to 1500. The ion spray voltage was set at 1.8 kV. The tandem mass spectrometry (MS/MS) analysis was performed by automatic switching between MS and MS/MS modes at collision energy 35%. To detect peptides containing GPI-glycan, mass spectrometry was performed using hydrophilic column. The samples were purified with Nu-Tip poly-HydroxyethylA (HILIC) tips (GlySci) according to the manu-facturer's protocol. Purified samples were then dissolved in 0.1% formic acid for measurement. Data were collected in positive ion mode on a nanoLC system using an EX-Nano Inert Sustain Amide capillary (0.1 × 150 mm; particle size, 3 µm) coupled to the same mass spectrometer. Measurement samples were injected onto the column by loop-injection method. The mobile phase was the same as above, and pep-tides were eluted by a gradient of 90% solvent B for 2 min followed by elution with a gradient of 5% solvent B for 22 min. The same MS parameter of mass spectrometry was used as described above. The obtained mass data were analyzed by Xcalibur (Proteome Discoverer1.4 Ver. 1.4.0.288) and peptides were identified by MASCOT Server ver2.7 (2.7.0) (Matrix Science) using the SwissProt_2021_02 data base (564,638 se-quences; 203,519,613 residues; taxonomy: *Mus musculus* [house mouse] [17,080 sequences]). Protease specificity was set for trypsin (C-term, KR; Restrict, P; Independent, no; Semi-specific, no; one missed and/or nonspecific cleavages permitted). Fixed modification considered was carbamido-methyl cysteine, and variable modifications considered were acetyl N terminus, N-terminal Gln to pyro-Glu, and oxidation of methionine. The peak intensity of each peptide corre-sponding to peptide with GPI-glycans was used for quantification.

Transmission experiments of prion strains

A mouse-adapted scrapie prion strain Chandler (50) was kindly provided by Dr Motohiro Horiuchi. A mouse-adapted GSS syndrome prion strain Fukuoka-1 (49) was maintained in C57BL/6 mice. The inocula were prepared from the brain of terminally ill mice. Intracerebral inoculation was performed as described (72). Briefly, 10% homogenates were prepared from the brain of terminally ill mice with one of the strains as inocula in sterile phosphate-buffered saline (PBS) using glass homogenizers, and 20 µl of the homogenates were intracere-brally inoculated into mice ($n = 6$). The inoculated mice were sacrificed at a predefined clinical endpoint, or at the time point showing intercurrent illness. To directly investigate whether

the conversion of PrP^{C} to PrP^{Sc} is accelerated in PGAP4-KO mice, Fukuoka-1-inoculated mice were also sacrificed at 50 dpi. One hemisphere of the brain was fixed in 10% buffered formalin for histopathological analysis, and the other hemi-sphere was immediately frozen for biochemical analysis.

Analysis of proteinase K–resistant PrP^{Sc}

For detection of PrP^{Sc} by Western blotting, samples were prepared as described (73). Briefly, brain tissues were homoge-nized in 2 ml of lysis buffer (100 mM Tris-HCl [pH 8.0], 10 mM NaCl, 10 mM MgCl$_2$, 2% Triton X-100, and 25 units/ml DNase I [Takara Bio]) and digested with collagenase (1 mg/200 mg tissue) (FUJIFILM Wako) overnight at room temperature. Collagenase digestion disrupts the connective tissue and improves the accessibility of detergents and/or proteinase K (PK) to PrP^{Sc} (74). The digested homogenates were ultracentrifuged at 453,000g for 30 min at 4 °C, and the pellets were resuspended and sonicated in 870 µl of PK digestion buffer (100 mM Tris-HCl pH 8.0 and 5% Sarkosyl [Sigma-Aldrich]). The resuspended samples were centrifuged at 10,000g for 3 min to remove the cell debris, and the supernatants (800 µl) were digested with PK (4 µg/200 mg tissue) (FUJIFILM Wako) for 1 h at 37 °C. It has been reported that these conditions for PK digestion were sufficient for the complete digestion of normal PrP^{C} and that higher PK concentrations caused unfavorable degradation of PrP^{Sc} (75). The PK-digested proteins were precipitated by adding 200 µl of 99.5% ethanol and ultracentrifugation at 135,000g for 30 min at 4 °C. The pellets were resuspended in 400 µl/200 mg tissue of 1 × Laemmli's SDS sample buffer and incubated at 100 °C for 5 min.

Immunofluorescence, RNAscope in situ hybridization, and immunohistochemistry

WT and PGAP4-KO mice were anesthetized by isoflurane and perfused with 20 ml of PBS followed by fixation with 20 ml of 4% paraformaldehyde in PBS. The brains were removed and immersed in the same fixative at 4 °C overnight. The brains were then cryoprotected in 20% sucrose solution at 4 °C for 3 to 4 days. Meanwhile, the solution was replaced with a fresh one every day. The cryo floating sections with 30-µm thickness were obtained and used for immunofluorescence staining. The sections were permeabilized and blocked with blocking buffer (3% bovine serum albumin, 0.1% NP-40 in PBS) at room temperature for 15 min and were incubated with blocking buffer containing the primary antibodies at 4 °C overnight, followed by further incubation with blocking buffer containing the secondary antibodies at room temperature for 1 h. The sections were mounted on the slide glass by Prolong diamond (ThermoFisher Scientific) antifade reagent. Fluorescence im-ages were obtained using a BZX-800 (KEYENCE) with sectioning function. Dilution rates of antibodies were as fol-lows: anti-GFP (1:200); anti-NeuN (1:200); anti-GFAP (1:200); goat anti-Iba1 (1:100); anti-rabbit IgG-Alexa488 (1:1000); anti-mouse IgG-Alexa546 (1:1000); anti-rat IgG-Alexa546 (1:1000); anti-goat IgG-Alexa546 (1:1000); DAPI (1:5000).

For double staining with *in situ* hybridization (ISH) and immunohistochemistry (IHC), the mice were perfused with 10% neutral buffered formalin and dissected. The brain tissues

were fixed in 10% neutral buffered formalin overnight. Paraffin-embedded tissues were cut into 3-μm-thick serial sections, deparaffinized, and stained with hematoxylin and eosin or used for ISH and IHC analysis. Dual ISH and IHC of the mouse tissue sections was performed using the RNA-Protein Co-Detection Ancillary Kit and RNAscope 2.5 High Definition (HD)—Red kit (#Cat No. 323180 and 322350, respectively; ACD) in accordance with the manufacturer's protocol. Briefly, on the first day, the sections were rinsed and blocked with 3% hydrogen peroxide in methanol for 10 min to remove endogenous peroxidase. After washing in distilled water (DW), the sections were incubated at 98 to 102 °C in Co-Detection Target Retrieval Reagents (supplied with the RNA-Protein Co-Detection Ancillary Kit) for 15 min. Then, the sections were incubated overnight at 4 °C with primary antibody against GFP (diluted 1:100; Abcam). On the second day, the sections were incubated at room temperature (RT) in 10% neutral buffered formalin. After washing in PBS, the sections were incubated with two drops of Protease Plus solution (supplied with RNAscope 2.5 High Definition (HD)—Red kit) for 30 min at 40 °C using the HybEZ Oven (Cat no. 310010, ACD). The slides were then washed twice with DW and hybridized with two drops of Mm-B3galt4 (Cat no. 839901, ACD), or DapB (Cat No. 310043, ACD), or Mm-Ppib (Cat no. 313911-C2, ACD) probes for 2 h at 40 °C, washed with wash buffer (WB) two times for 2 min each (hereinafter referred to as WB 2 × 2), incubated with two drops of AMP-1 (all the AMP are from the Detection kit, Cat no. 322350, ACD) for 30 min at 40 °C, washed with WB 2 × 2, incubated with two drops of AMP-2 for 15 min at 40 °C, washed in WB 2 × 2, incubated with two drops of AMP-3 for 30 min at 40 °C, washed with WB 2 × 2, incubated with two drops of AMP-4 for 15 min at 40 °C, washed with WB 2 × 2, incubated with two drops of AMP-5 for 30 min at RT, washed with WB 2 × 2, incubated with two drops of AMP-6 for 15 min at RT, and washed with WB 2 × 2. Then, the Fast-RED was used for 10 min at RT and washed with DW and WB 2 × 2. The sections were incubated with Co-Detection Blocker solution (supplied with the RNA-Protein Co-Detection Ancillary Kit) for 15 min at 40 °C and washed with WB 2 × 2 and PBS 2 × 2. The sections were incubated at RT for 60 min and washed with PBS 2 × 2. The bound complex was visualized using SIG-MAFAST 3,3′-diaminobenzidine tablets (Cat. no. D4293; Sigma-Aldrich) and counterstained with hematoxylin. Finally, the sections were mounted with Mounting media.

For immunohistochemistry of PrP^{Sc}-infected mouse brains, 10% formalin-fixed mouse brain tissues were treated with 60% formic acid for 1 h to inactivate the infectivity and embedded in paraffin. The embedded tissues were sectioned at a thickness of 5 μm. Tissue sections were pretreated by hydrolytic autoclaving before PrP immunohistochemistry [76]. The anti-PrP antiserum PrP-N [77], rabbit anti-Iba1 polyclonal antibody (FUJIFILM Wako), and rabbit anti-GFAP polyclonal antibody (Dako) were used as the primary antibodies. Goat anti-rabbit IgG polyclonal antibody labeled with the peroxidase-conjugated dextran polymer, EnVision$^+$ (Dako), was used as the secondary antibody.

Clinical tests

Hematological test

Nine-week-old male and female mice were used for the study. Blood, 200 μl, was collected from the retro-orbital sinus using a Pasteur pipette (ThermoFisher Scientific). To avoid coagulation of the blood, the collected blood was transferred to microtubes containing 8 μl of 10% EDTA solution, and the number of blood cells including erythrocytes, leucocytes, red blood cells, and reticulocytes was measured by ADVIA2120i system (SIEMENS).

Clinical biochemical test

Eleven-week-old male and female mice were used and the blood was collected as described above. The collected blood was transferred to Heparin-Lithium coated tube, and serum was separated by centrifugation twice at 5000g for 10 min at 8 °C. We measured total protein, albumin, total cholesterol, and so on in the serum with an automatic clinical biochemistry analyzer (JCA-BM6070) (JEOL Ltd).

Urinalysis test

Ten-week-old male and female mice were used. The mice were restrained and allowed to urinate on the tray. A sufficient amount of urine was absorbed with the urine test paper (Arkray Aution Sticks 7EA, purchased from Arkray), and the test paper was placed in a horizontal position for 1 min, followed by comparison of the color of the test paper to the color scale sheet attached to the test paper container.

Investigation of body composition

Twenty-two-week-old male and female mice were used. Mice were anesthetized by intraperitoneal injection of anesthetic solution. When the mice became unconsciousness, they were placed into the PIXImus2 analyzer (Lunar, GE Healthcare) and body composition was measured.

X-ray analyses

Twenty-two-week-old male and female mice were used. Mice were anesthetized and mounted in a prone position onto the X-ray plate for the dorsoventral view, and the tail was curved along the left side of the mouse. The X-ray plate was inserted into the Faxitron X-ray system (MX-20-DC12, Faxitron X-Ray corporation) and the machine was set to a voltage of 26 kV, with an exposure time of 10 s. Images of the dorsoventral view were taken using the Faxitron DX software. The anesthetized mice were mounted sideways onto another X-ray plate for the lateral orientation view, and the tail was curved along the dorsal side of the mouse. The images were taken as described above. Sixty-one items related to bone characteristics were recorded.

Funduscopic analyses

Nineteen-week-old male and female mice were used. Mydrin P (Santen Pharmaceutical Co) diluted 5 to 7.5 times with physiological saline was applied to the eye of the mouse. After the pupil was dilated, the position of the mouse was

adjusted to take the photographs. The photographs were taken by Genesis hand funduscopy camera (Kowa Company) with a Vlk 90D lens.

Electrocardiogram

Twenty-four-week-old male and female mice were used. The mice were held by hand gently on which the lead platelet surface electrode is set at palms and sole with plastic clips and connected to the preamplifier unit. The platelet surface electrode was covered with conducting cream to ensure close contact on their skin. Then, electrocardiogram was recorded.

Immunophenotyping test

Twenty-six-week-old male and female mice were used. The spleen was collected from euthanized mice and minced into pieces using scissors. The samples were incubated with 3 ml of $1 \times$ enzyme cocktail (containing 10 mM Hepes, 2% fetal bovine serum, 200 Mandl Units/ml collagenase D, and 0.01 mg/ml DNAse I in HBSS with Ca^{2+} and Mg^{2+}) in a 37 °C water bath for 20 min. Cell suspension was filtered through a nylon mesh into 12×75-mm tube, followed by centrifugation at $500g$ in a swing bucket roto for 5 min at 10 °C. The pellet was resuspended with 2 ml FACS buffer (containing 10 mM Hepes, 2% fetal bovine serum, and 2 mM EDTA in PBS without Ca^{2+} and Mg^{2+}) by vortexing. After cell counting, 4×10^6 cells were used and red blood cells (RBCs) were lysed with 50 µl of $1 \times$ RBC lysis buffer (obtained by dilution of $10 \times$ RBC lysis buffer [eBioscience]) by incubating for 1 min at room temperature. After adding 100 µl of FACS buffer, cells were precipitated by centrifugation at $510g$ for 2 min at 4 °C. The pellet was resuspended in 100 µl of Fc blocking antibody (diluted by 50 times) and incubated on ice for 10 min. After centrifugation at $510g$ for 2 min at 4 °C, the pellet was resuspended in 50 µl of antibody cocktail, followed by incubation on ice and in the dark for 60 min. After incubation, 100 µl of FACS buffer was added and cell pellet was precipitated by centrifugation at $510g$ for 2 min at 4 °C. The pellet was resuspended in 200 µl of read buffer (SytoxBlue [ThermoFisher Scientific] diluted by 10,000 times in FACS buffer). The data were collected by FACS LSRFortessa (BD Biosciences) and analyzed using FlowJo software (BD Biosciences).

Behavior tests

All behavior tests were carried out in the Japan Mouse Clinic, RIKEN BioResource Center. Seven WT and PGAP4-KO male mice were used for all the behavior tests. For all tests, the mice were transferred from their home cages to the testing room at least 30 min before the experiments.

Open field test

Seven-week-old mice were used for the study. Each mouse was gently placed in a corner of an open-field apparatus made of white polyvinyl chloride (40 cm wide × 40 cm long × 32 cm height) (O'Hara & Co). The distance traveled by each animal in the open field was recorded for 20 min with a video-imaging system (Image OF9) (O'Hara & Co) mounted above the center of the open field.

Home cage activity test

Ten-week-old mice were used. Each mouse was placed alone in a testing cage (22.7 × 32.9 × 13.3 cm) under a 12-h light–dark cycle (light on at 8:00 AM) and had free access to both food and water. After 1 day of habituation, spontaneous activity in the cage was measured for 5 days (starting at 8:00 AM) using an infrared sensor (activity sensor) (O'Hara & Co). Home cage parameters included activity in light phase, activity in dark phase, total activity, and activity ratio between light phase and total.

Crawley's social interaction test

Nine-week-old mice were used. The apparatus comprised a rectangular, three-chambered box and a lid containing a video camera (O'Hara & Co) Each chamber was 20 × 40 × 22 cm, and the dividing walls were made from clear plexiglass, with small square openings (5 × 3 cm) allowing access into each chamber. The subject mouse was placed in the middle chamber of the test apparatus and allowed to explore the entire apparatus for a 10-min session 1 week before the test for habituation. After 1 week from the habituation, social novelty test was performed. Before the test, each mouse was habituated to the testing room for 15 min. The mice were then placed in the middle of the chamber and allowed to explore the entire apparatus for 10 min. To examine object exploration behavior of the subject mice, an inanimate object (colors and shape were different from the objects used in the object recognition task, Lego tower, 8 cm high, 4 cm wide, 3.2 cm depth, build in red, yellow, orange, black, green, light green, blue, and white bricks) was placed in a wire cage in one side of the chamber. The total time spent near each cage (<4.5 cm) during a 10-min period was determined with a video-imaging system (Time CSI2) (O'Hara & Co). As for social interaction test, the inanimate object was replaced with a stranger mouse (male C57BL/6J) and the total time spent near each cage (<4.5 cm) during a 10-min period was determined.

Fear conditioning test

Thirteen-week-old mice were used. We used automated fear contextual and tone-dependent fear conditioning apparatus, Image FZ4 (O'Hara & Co). For conditioning at day 1, each mouse was placed in a shock chamber (white wall [box A]) for 120 s as habituation. After the habituation, four tone-shock pairs were given at 90-s intervals. The tone-shock pair consists of tone (70 db, 10 kHz) for 30 s and a foot shock of 0.5 s at 0.5 mA. The foot shock was presented to mice during the last 0.5 s of the tone. For contextual testing at day 2, each mouse was placed back in box A for 6 min and contextual freezing was measured approximately 24 h after conditioning. For cued test at day 3, approximately 24 h after contextual testing, each mouse was placed in a transparent chamber (box B, which is different from box A) for 120 s to measure baseline data. After the measurement of baseline data, freezing during the tone presentation was measured as the response to the tone.

Prepulse inhibition test

Fourteen-week-old mice were used. Load cell, mouse chamber, sound generator, and sound-proof box (33 cm length × 43 cm width × 33 cm height) were purchased from O'Hara & Co. Before each testing session, mechanical responses were calibrated. The mouse was acclimated to chamber for 5 min (only 65 dB background noise was on). During this period, 110 dB/40 ms of white noise was presented for five times to acclimate mice to startle pulse. Startle response to these stimuli were excluded from the statistical analysis. Prepulse sounds (70, 75, 80, 85 dB for 20 msec) and a startle sound (110 dB for 50 msec) were presented 10 times in pseudorandom order, with an inner-trial interval varying randomly between 10 and 20 s, and startle amplitude was measured 50 msec after presentation of the prepulse sound. Percentage of PPI was calculated as [(startle amplitude without prepulse) − (startle amplitude of trial with prepulse)]/(startle amplitude without prepulse) × 100.

Statistics

Statistics were performed using GraphPad Prism 8 software (GraphPad Software, Inc).

Data availability

LC-MS data of PrP^C GPI in WT and PGAP4-KO mice has been deposited in PRIDE database. Data are available *via* ProteomeXchange with identifier PXD029190 (WT) and PXD029189 (PGAP4-KO).

Abbreviations—The abbreviations used are: 2ME, 2-mercaptethanol; ALP, alkaline phosphatase; DRM, detergent-resistant membrane; DW, distilled water; ER, endoplasmic reticulum; ES, embryonic stem; GPI, glycosylphosphatidylinositol; GPI-AP, GPI-anchored protein; GSS, Gerstmann–Sträussler–Scheinker; HRP, horse radish peroxidase; IGD, inherited GPI deficiency; IHC, immunohistochemistry; ISH, *in situ* hybridization; MS, mass spectrometry; PK, proteinase K; PrP^C, prion protein; PrP^{Sc}, scrapie form of the prion protein; RBC, red blood cell; TBS, Tris-buffered saline; WB, wash buffer.

References

1. Kinoshita, T. (2020) Biosynthesis and biology of mammalian GPI-anchored proteins. *Open Biol.* **10**, 190290
2. Liu, Y. S., and Fujita, M. (2020) Mammalian GPI-anchor modifications and the enzymes involved. *Biochem. Soc. Trans.* **48**, 1129–1138
3. Ferguson, M. A. J., Hart, G. W., and Kinoshita, T. (2015) Glycosylphosphatidylinositol anchors. In: Varki, A., Cummings, R. D., Esko, J. D., Stanley, P., Hart, G. W., Aebi, M., Darvill, A. G., Kinoshita, T., Packer, N. H., Prestegard, J. H., Schnaar, R. L., Seeberger, P. H., eds. *Essentials of Glycobiology*, Cold Spring Hobor Laboratory Press, Cold Spring Harbor, NY: 137–150
4. Taron, B. W., Colussi, P. A., Wiedman, J. M., Orlean, P., and Taron, C. H. (2004) Human Smp3p adds a fourth mannose to yeast and human glycosylphosphatidylinositol precursors *in vivo*. *J. Biol. Chem.* **279**, 36083–36092
5. Homans, S. W., Ferguson, M. A., Dwek, R. A., Rademacher, T. W., Anand, R., and Williams, A. F. (1988) Complete structure of the glycosyl phosphatidylinositol membrane anchor of rat brain Thy-1 glycoprotein. *Nature* **333**, 269–272
6. Stahl, N., Baldwin, M. A., Hecker, R., Pan, K. M., Burlingame, A. L., and Prusiner, S. B. (1992) Glycosylinositol phospholipid anchors of the scrapie and cellular prion proteins contain sialic acid. *Biochemistry* **31**, 5043–5053
7. Kobayashi, A., Hirata, T., Nishikaze, T., Ninomiya, A., Maki, Y., Takada, Y., Kitamoto, T., and Kinoshita, T. (2020) alpha2,3 Linkage of sialic acid to a GPI anchor and an unpredicted GPI attachment site in human prion protein. *J. Biol. Chem.* **295**, 7789–7798
8. Hirata, T., Mishra, S. K., Nakamura, S., Saito, K., Motooka, D., Takada, Y., Kanzawa, N., Murakami, Y., Maeda, Y., Fujita, M., Yamaguchi, Y., and Kinoshita, T. (2018) Identification of a Golgi GPI-N-acetylgalactosamine transferase with tandem transmembrane regions in the catalytic domain. *Nat. Commun.* **9**, 405
9. Wang, Y., Maeda, Y., Liu, Y. S., Takada, Y., Ninomiya, A., Hirata, T., Fujita, M., Murakami, Y., and Kinoshita, T. (2020) Cross-talks of glycosylphosphatidylinositol biosynthesis with glycosphingolipid biosynthesis and ER-associated degradation. *Nat. Commun.* **11**, 860
10. Miyazaki, H., Fukumoto, S., Okada, M., Hasegawa, T., and Furukawa, K. (1997) Expression cloning of rat cDNA encoding UDP-galactose:GD2 beta1,3-galactosyltransferase that determines the expression of GD1b/GM1/GA1. *J. Biol. Chem.* **272**, 24794–24799
11. Amado, M., Almeida, R., Carneiro, F., Levery, S. B., Holmes, E. H., Nomoto, M., Hollingsworth, M. A., Hassan, H., Schwientek, T., Nielsen, P. A., Bennett, E. P., and Clausen, H. (1998) A family of human beta3-galactosyltransferases. Characterization of four members of a UDP-galactose:beta-N-acetyl-glucosamine/beta-nacetyl-galactosamine beta-1, 3-galactosyltransferase family. *J. Biol. Chem.* **273**, 12770–12778

12. Nozaki, M., Ohishi, K., Yamada, N., Kinoshita, T., Nagy, A., and Takeda, J. (1999) Developmental abnormalities of glycosylphosphatidylinositol-anchor-deficient embryos revealed by Cre/loxP system. *Lab. Invest.* **79**, 293–299

13. Ueda, Y., Yamaguchi, R., Ikawa, M., Okabe, M., Morii, E., Maeda, Y., and Kinoshita, T. (2007) PGAP1 knock-out mice show otocephaly and male infertility. *J. Biol. Chem.* **282**, 30373–30380

14. Zoltewicz, J. S., Ashique, A. M., Choe, Y., Lee, G., Taylor, S., Phamluong, K., Solloway, M., and Peterson, A. S. (2009) Wnt signaling is regulated by endoplasmic reticulum retention. *PLoS One* **4**, e6191

15. McKean, D. M., and Niswander, L. (2012) Defects in GPI biosynthesis perturb Cripto signaling during forebrain development in two new mouse models of holoprosencephaly. *Biol. Open* **1**, 874–883

16. Lukacs, M., Roberts, T., Chatuverdi, P., and Stottmann, R. W. (2019) Glycosylphosphatidylinositol biosynthesis and remodeling are required for neural tube closure, heart development, and cranial neural crest cell survival. *Elife* **8**, e45248

17. Murakami, H., Wang, Y., Hasuwa, H., Maeda, Y., Kinoshita, T., and Murakami, Y. (2012) Enhanced response of T lymphocytes from Pgap3 knockout mouse: Insight into roles of fatty acid remodeling of GPI anchored proteins. *Biochem. Biophys. Res. Commun.* **417**, 1235–1241

18. Lukacs, M., Blizzard, L. E., and Stottmann, R. W. (2020) CNS glycosylphosphatidylinositol deficiency results in delayed white matter development, ataxia and premature death in a novel mouse model. *Hum. Mol. Genet.* **29**, 1205–1217

19. Rodriguez de Los Santos, M., Rivalan, M., David, F. S., Stumpf, A., Pitsch, J., Tsortouktzidis, D., Velasquez, L. M., Voigt, A., Schilling, K., Mattei, D., Long, M., Vogt, G., Knaus, A., Fischer-Zirnsak, B., Wittler, L., *et al.* (2021) A CRISPR-Cas9-engineered mouse model for GPI-anchor deficiency mirrors human phenotypes and exhibits hippocampal synaptic dysfunctions. *Proc. Natl. Acad. Sci. U. S. A.* **118**, e2014481118

20. Knaus, A., Pantel, J. T., Pendziwiat, M., Hajjir, N., Zhao, M., Hsieh, T. C., Schubach, M., Gurovich, Y., Fleischer, N., Jager, M., Kohler, S., Muhle, H., Korff, C., Moller, R. S., Bayat, A., *et al.* (2018) Characterization of glycosylphosphatidylinositol biosynthesis defects by clinical features, flow cytometry, and automated image analysis. *Genome Med.* **10**, 3

21. Bellai-Dussault, K., Nguyen, T. T. M., Baratang, N. V., Jimenez-Cruz, D. A., and Campeau, P. M. (2019) Clinical variability in inherited glycosylphosphatidylinositol deficiency disorders. *Clin. Genet.* **95**, 112–121

22. Johnston, J. J., Gropman, A. L., Sapp, J. C., Teer, J. K., Martin, J. M., Liu, C. F., Yuan, X., Ye, Z., Cheng, L., Brodsky, R. A., and Biesecker, L. G. (2012) The phenotype of a germline mutation in PIGA: The gene somatically mutated in paroxysmal nocturnal hemoglobinuria. *Am. J. Hum. Genet.* **90**, 295–300

23. Knaus, A., Kortum, F., Kleefstra, T., Stray-Pedersen, A., Dukic, D., Murakami, Y., Gerstner, T., van Bokhoven, H., Iqbal, Z., Horn, D., Kinoshita, T., Hempel, M., and Krawitz, P. M. (2019) Mutations in PIGU impair the function of the GPI transamidase complex, causing severe intellectual disability, epilepsy, and brain anomalies. *Am. J. Hum. Genet.* **105**, 395–402

24. Murakami, Y., Nguyen, T. T. M., Baratang, N., Raju, P. K., Knaus, A., Ellard, S., Jones, G., Lace, B., Rousseau, J., Ajeawung, N. F., Kamei, A., Minase, G., Akasaka, M., Araya, N., Koshimizu, E., *et al.* (2019) Mutations in PIGB cause an inherited GPI biosynthesis defect with an axonal neuropathy and metabolic abnormality in severe cases. *Am. J. Hum. Genet.* **105**, 384–394

25. Ng, B. G., Hackmann, K., Jones, M. A., Eroshkin, A. M., He, P., Wiliams, R., Bhide, S., Cantagrel, V., Gleeson, J. G., Paller, A. S., Schnur, R. E., Tinschert, S., Zunich, J., Hegde, M. R., and Freeze, H. H. (2012) Mutations in the glycosylphosphatidylinositol gene PIGL cause CHIME syndrome. *Am. J. Hum. Genet.* **90**, 685–688

26. Murakami, Y., Tawamie, H., Maeda, Y., Buttner, C., Buchert, R., Radwan, F., Schaffer, S., Sticht, H., Aigner, M., Reis, A., Kinoshita, T., and Jamra, R. A. (2014) Null mutation in PGAP1 impairing Gpi-anchor maturation in patients with intellectual disability and encephalopathy. *PLoS Genet.* **10**, e1004320

27. Horn, D., Wieczorek, D., Metcalfe, K., Baric, I., Palezac, L., Cuk, M., Petkovic Ramadza, D., Kruger, U., Demuth, S., Heinritz, W., Linden, T.,

Koenig, J., Robinson, P. N., and Krawitz, P. (2014) Delineation of PIGV mutation spectrum and associated phenotypes in hyperphosphatasia with mental retardation syndrome. *Eur. J. Hum. Genet.* **22**, 762–767

28. Prusiner, S. B. (1998) Prions. *Proc. Natl. Acad. Sci. U. S. A.* **95**, 13363–13383

29. Prusiner, S. B., Scott, M. R., DeArmond, S. J., and Cohen, F. E. (1998) Prion protein biology. *Cell* **93**, 337–348

30. Pan, K. M., Baldwin, M., Nguyen, J., Gasset, M., Serban, A., Groth, D., Mehlhorn, I., Huang, Z., Fletterick, R. J., Cohen, F. E., and Prusiner, S. B. (1993) Conversion of alpha-helices into beta-sheets features in the formation of the scrapie prion proteins. *Proc. Natl. Acad. Sci. U. S. A.* **90**, 10962–10966

31. Bueler, H., Aguzzi, A., Sailer, A., Greiner, R. A., Autenried, P., Aguet, M., and Weissmann, C. (1993) Mice devoid of PrP are resistant to scrapie. *Cell* **73**, 1339–1347

32. Prusiner, S. B., Groth, D., Serban, A., Koehler, R., Foster, D., Torchia, M., Burton, D., Yang, S. L., and DeArmond, S. J. (1993) Ablation of the prion protein (PrP) gene in mice prevents scrapie and facilitates production of anti-PrP antibodies. *Proc. Natl. Acad. Sci. U. S. A.* **90**, 10608–10612

33. Mallucci, G., Dickinson, A., Linehan, J., Klohn, P. C., Brandner, S., and Collinge, J. (2003) Depleting neuronal PrP in prion infection prevents disease and reverses spongiosis. *Science* **302**, 871–874

34. Sandberg, M. K., Al-Doujaily, H., Sharps, B., Clarke, A. R., and Collinge, J. (2011) Prion propagation and toxicity *in vivo* occur in two distinct mechanistic phases. *Nature* **470**, 540–542

35. Puig, B., Altmeppen, H., and Glatzel, M. (2014) The GPI-anchoring of PrP: Implications in sorting and pathogenesis. *Prion* **8**, 11–18

36. Chesebro, B., Trifilo, M., Race, R., Meade-White, K., Teng, C., LaCasse, R., Raymond, L., Favara, C., Baron, G., Priola, S., Caughey, B., Masliah, E., and Oldstone, M. (2005) Anchorless prion protein results in infectious amyloid disease without clinical scrapie. *Science* **308**, 1435–1439

37. Rangel, A., Race, B., Phillips, K., Striebel, J., Kurtz, N., and Chesebro, B. (2014) Distinct patterns of spread of prion infection in brains of mice expressing anchorless or anchored forms of prion protein. *Acta Neuropathol. Commun.* **2**, 8

38. Chesebro, B., Race, B., Meade-White, K., Lacasse, R., Race, R., Klingeborn, M., Striebel, J., Dorward, D., McGovern, G., and Jeffrey, M. (2010) Fatal transmissible amyloid encephalopathy: A new type of prion disease associated with lack of prion protein membrane anchoring. *PLoS Pathog.* **6**, e1000800

39. Bate, C., Nolan, W., and Williams, A. (2016) Sialic acid on the glycosylphosphatidylinositol anchor regulates PrP-mediated cell signaling and prion formation. *J. Biol. Chem.* **291**, 160–170

40. Puig, B., Altmeppen, H. C., Linsenmeier, L., Chakroun, K., Wegwitz, F., Piontek, U. K., Tatzelt, J., Bate, C., Magnus, T., and Glatzel, M. (2019) GPI-anchor signal sequence influences PrPC sorting, shedding and signalling, and impacts on different pathomechanistic aspects of prion disease in mice. *PLoS Pathog.* **15**, e1007520

41. Cong, L., Ran, F. A., Cox, D., Lin, S., Barretto, R., Habib, N., Hsu, P. D., Wu, X., Jiang, W., Marraffini, L. A., and Zhang, F. (2013) Multiplex genome engineering using CRISPR/Cas systems. *Science* **339**, 819–823

42. Mali, P., Yang, L., Esvelt, K. M., Aach, J., Guell, M., DiCarlo, J. E., Norville, J. E., and Church, G. M. (2013) RNA-guided human genome engineering *via* Cas9. *Science* **339**, 823–826

43. Wang, Y., Hirata, T., Maeda, Y., Murakami, Y., Fujita, M., and Kinoshita, T. (2019) Free, unlinked glycosylphosphatidylinositols on mammalian cell surfaces revisited. *J. Biol. Chem.* **294**, 5038–5049

44. Balcerzak, M., Hamade, E., Zhang, L., Pikula, S., Azzar, G., Radisson, J., Bandorowicz-Pikula, J., and Buchet, R. (2003) The roles of annexins and alkaline phosphatase in mineralization process. *Acta Biochim. Pol.* **50**, 1019–1038

45. Hessle, L., Johnson, K. A., Anderson, H. C., Narisawa, S., Sali, A., Goding, J. W., Terkeltaub, R., and Millan, J. L. (2002) Tissue-nonspecific alkaline phosphatase and plasma cell membrane glycoprotein-1 are central antagonistic regulators of bone mineralization. *Proc. Natl. Acad. Sci. U. S. A.* **99**, 9445–9449

46. Fedde, K. N., Blair, L., Silverstein, J., Coburn, S. P., Ryan, L. M., Weinstein, R. S., Waymire, K., Narisawa, S., Millan, J. L., MacGregor, G. R., and

Whyte, M. P. (1999) Alkaline phosphatase knock-out mice recapitulate the metabolic and skeletal defects of infantile hypophosphatasia. *J. Bone Miner. Res.* **14**, 2015–2026

47. Phillips, R. G., and LeDoux, J. E. (1992) Differential contribution of amygdala and hippocampus to cued and contextual fear conditioning. *Behav. Neurosci.* **106**, 274–285

48. Michalovicz, L. T., Kelly, K. A., Vashishtha, S., Ben-Hamo, R., Efroni, S., Miller, J. V., Locker, A. R., Sullivan, K., Broderick, G., Miller, D. B., and O'Callaghan, J. P. (2019) Astrocyte-specific transcriptome analysis using the ALDH1L1 bacTRAP mouse reveals novel biomarkers of astrogliosis in response to neurotoxicity. *J. Neurochem.* **150**, 420–440

49. Tateishi, J., Ohta, M., Koga, M., Sato, Y., and Kuroiwa, Y. (1979) Transmission of chronic spongiform encephalopathy with kuru plaques from humans to small rodents. *Ann. Neurol.* **5**, 581–584

50. Chandler, R. L. (1961) Encephalopathy in mice produced by inoculation with scrapie brain material. *Lancet* **1**, 1378–1379

51. Mukasa, R., Umeda, M., Endo, T., Kobata, A., and Inoue, K. (1995) Characterization of glycosylphosphatidylinositol (GPI)-anchored NCAM on mouse skeletal muscle cell line C2C12: The structure of the GPI glycan and release during myogenesis. *Arch. Biochem. Biophys.* **318**, 182–190

52. Brewis, I. A., Ferguson, M. A., Mehlert, A., Turner, A. J., and Hooper, N. M. (1995) Structures of the glycosyl-phosphatidylinositol anchors of porcine and human renal membrane dipeptidase. Comprehensive structural studies on the porcine anchor and interspecies comparison of the glycan core structures. *J. Biol. Chem.* **270**, 22946–22956

53. Wang, Y., Murakami, Y., Yasui, T., Wakana, S., Kikutani, H., Kinoshita, T., and Maeda, Y. (2013) Significance of glycosylphosphatidylinositol-anchored protein enrichment in lipid rafts for the control of autoimmunity. *J. Biol. Chem.* **288**, 25490–25499

54. Howard, M. F., Murakami, Y., Pagnamenta, A. T., Daumer-Haas, C., Fischer, B., Hecht, J., Keays, D. A., Knight, S. J., Kolsch, U., Kruger, U., Leiz, S., Maeda, Y., Mitchell, D., Mundlos, S., Phillips, J. A., 3rd, *et al.* (2014) Mutations in PGAP3 impair GPI-anchor maturation, causing a subtype of hyperphosphatasia with mental retardation. *Am. J. Hum. Genet.* **94**, 278–287

55. Murakami, Y., Kanzawa, N., Saito, K., Krawitz, P. M., Mundlos, S., Robinson, P. N., Karadimitris, A., Maeda, Y., and Kinoshita, T. (2012) Mechanism for release of alkaline phosphatase caused by glycosylphosphatidylinositol deficiency in patients with hyperphosphatasia mental retardation syndrome. *J. Biol. Chem.* **287**, 6318–6325

56. Karp, N. A., Mason, J., Beaudet, A. L., Benjamini, Y., Bower, L., Braun, R. E., Brown, S. D. M., Chesler, E. J., Dickinson, M. E., Flenniken, A. M., Fuchs, H., Angelis, M. H., Gao, X., Guo, S., Greenaway, S., *et al.* (2017) Prevalence of sexual dimorphism in mammalian phenotypic traits. *Nat. Commun.* **8**, 15475

57. Tan, R. P. A., Leshchyns'ka, I., and Sytnyk, V. (2017) Glycosylphosphatidylinositol-anchored immunoglobulin superfamily cell adhesion molecules and their role in neuronal development and synapse regulation. *Front. Mol. Neurosci.* **10**, 378

58. Kasahara, K., Watanabe, K., Kozutsumi, Y., Oohira, A., Yamamoto, T., and Sanai, Y. (2002) Association of GPI-anchored protein TAG-1 with src-family kinase Lyn in lipid rafts of cerebellar granule cells. *Neurochem. Res.* **27**, 823–829

59. Iskandar, B. J., Rizk, E., Meier, B., Hariharan, N., Bottiglieri, T., Finnell, R. H., Jarrard, D. F., Banerjee, R. V., Skene, J. H., Nelson, A., Patel, N., Gherasim, C., Simon, K., Cook, T. D., and Hogan, K. J. (2010) Folate regulation of axonal regeneration in the rodent central nervous system through DNA methylation. *J. Clin. Invest.* **120**, 1603–1616

60. Egea, J., and Klein, R. (2007) Bidirectional Eph-ephrin signaling during axon guidance. *Trends Cell Biol* **17**, 230–238

61. de Wit, J., O'Sullivan, M. L., Savas, J. N., Condomitti, G., Caccese, M. C., Vennekens, K. M., Yates, J. R., 3rd, and Ghosh, A. (2013) Unbiased discovery of glypican as a receptor for LRRTM4 in regulating excitatory synapse development. *Neuron* **79**, 696–711

62. Siddiqui, T. J., Tari, P. K., Connor, S. A., Zhang, P., Dobie, F. A., She, K., Kawabe, H., Wang, Y. T., Brose, N., and Craig, A. M. (2013) An LRRTM4-HSPG complex mediates excitatory synapse development on dentate gyrus granule cells. *Neuron* **79**, 680–695

63. Qiu, S., Champagne, D. L., Peters, M., Catania, E. H., Weeber, E. J., Levitt, P., and Pimenta, A. F. (2010) Loss of limbic system-associated membrane protein leads to reduced hippocampal mineralocorticoid receptor expression, impaired synaptic plasticity, and spatial memory deficit. *Biol. Psychiatry* **68**, 197–204

64. Smith, H. L., Freeman, O. J., Butcher, A. J., Holmqvist, S., Humoud, I., Schatzl, T., Hughes, D. T., Verity, N. C., Swinden, D. P., Hayes, J., de Weerd, L., Rowitch, D. H., Franklin, R. J. M., and Mallucci, G. R. (2020) Astrocyte unfolded protein response induces a specific reactivity state that causes non-cell-autonomous neuronal degeneration. *Neuron* **105**, 855–866.e5

65. Moremen, K. W., Tiemeyer, M., and Nairn, A. V. (2012) Vertebrate protein glycosylation: Diversity, synthesis and function. *Nat. Rev. Mol. Cell Biol.* **13**, 448–462

66. Ran, F. A., Hsu, P. D., Wright, J., Agarwala, V., Scott, D. A., and Zhang, F. (2013) Genome engineering using the CRISPR-Cas9 system. *Nat. Protoc.* **8**, 2281–2308

67. Fujihara, Y., Kaseda, K., Inoue, N., Ikawa, M., and Okabe, M. (2013) Production of mouse pups from germline transmission-failed knockout chimeras. *Transgenic Res.* **22**, 195–200

68. Oji, A., Noda, T., Fujihara, Y., Miyata, H., Kim, Y. J., Muto, M., Nozawa, K., Matsumura, T., Isotani, A., and Ikawa, M. (2016) CRISPR/Cas9 mediated genome editing in ES cells and its application for chimeric analysis in mice. *Sci. Rep.* **6**, 31666

69. Tomavo, S., Couvreur, G., Leriche, M. A., Sadak, A., Achbarou, A., Fortier, B., and Dubremetz, J. F. (1994) Immunolocalization and characterization of the low molecular weight antigen (4-5 kDa) of Toxoplasma gondii that elicits an early IgM response upon primary infection. *Parasitology* **108**, 139–145

70. Striepen, B., Zinecker, C. F., Damm, J. B., Melgers, P. A., Gerwig, G. J., Koolen, M., Vliegenthart, J. F., Dubremetz, J. F., and Schwarz, R. T. (1997) Molecular structure of the "low molecular weight antigen" of Toxoplasma gondii: A glucose alpha 1-4 N-acetylgalactosamine makes free glycosyl-phosphatidylinositols highly immunogenic. *J. Mol. Biol.* **266**, 797–813

71. Asano, M., Mohri, S., Ironside, J. W., Ito, M., Tamaoki, N., and Kitamoto, T. (2006) vCJD prion acquires altered virulence through trans-species infection. *Biochem. Biophys. Res. Commun.* **342**, 293–299

72. Kitamoto, T., Mohri, S., Ironside, J. W., Miyoshi, I., Tanaka, T., Kitamoto, N., Itohara, S., Kasai, N., Katsuki, M., Higuchi, J., Muramoto, T., and Shin, R. W. (2002) Follicular dendritic cell of the knock-in mouse provides a new bioassay for human prions. *Biochem. Biophys. Res. Commun.* **294**, 280–286

73. Munesue, Y., Shimazaki, T., Qi, Z., Isoda, N., Sawa, H., Aoshima, K., Kimura, T., Mohri, S., Kitamoto, T., and Kobayashi, A. (2018) Development of a quick bioassay for the evaluation of transmission properties of acquired prion diseases. *Neurosci. Lett.* **668**, 43–47

74. Grathwohl, K. U., Horiuchi, M., Ishiguro, N., and Shinagawa, M. (1996) Improvement of PrPSc-detection in mouse spleen early at the preclinical stage of scrapie with collagenase-completed tissue homogenization and Sarkosyl-NaCl extraction of PrPSc. *Arch. Virol.* **141**, 1863–1874

75. Hizume, M., Kobayashi, A., Teruya, K., Ohashi, H., Ironside, J. W., Mohri, S., and Kitamoto, T. (2009) Human prion protein (PrP) 219K is converted to PrPSc but shows heterozygous inhibition in variant Creutzfeldt-Jakob disease infection. *J. Biol. Chem.* **284**, 3603–3609

76. Kitamoto, T., Shin, R. W., Doh-ura, K., Tomokane, N., Miyazono, M., Muramoto, T., and Tateishi, J. (1992) Abnormal isoform of prion proteins accumulates in the synaptic structures of the central nervous system in patients with Creutzfeldt-Jakob disease. *Am. J. Pathol.* **140**, 1285–1294

77. Kitamoto, T., Muramoto, T., Hilbich, C., Beyreuther, K., and Tateishi, J. (1991) N-terminal sequence of prion protein is also integrated into kuru plaques in patients with Gerstmann-Straussler syndrome. *Brain Res.* **545**, 319–321